

Numerical investigation of added resistance of a container ship in short regular waves using unsteady RANS simulations



Paresh Halder, Shukui Liu*

School of Mechanical and Aerospace Engineering, Nanyang Technological University, 50 Nanyang Avenue, 639798, Singapore

ARTICLE INFO

Keywords:

Added resistance in waves
diffraction
short waves
computational fluid dynamics

ABSTRACT

Accurately predicting the added resistance coefficient in short waves remains a challenge. This study aims to investigate the added resistance of a container ship in regular short-head waves at moderate Froude numbers through unsteady RANS simulations. A body-fitted, full-hexahedral unstructured mesh models the ship's motion, while the volume of fluid (VoF) method determines the free surface. Regular head waves of relatively short wavelengths, ranging from $0.22 \leq \lambda/L_{PP} \leq 0.65$, are considered in the simulations. The study first examines the stability of the generated waves, followed by an analysis of the wave field around the hull with the ship present, and an assessment of the numerical residual. Fast Fourier Transform (FFT) is applied to the non-dimensional longitudinal force in regular head waves to calculate the mean value of the added resistance. This is to remove the noise in the force signal. Detailed analyses of flow characteristics, including free-surface elevation and pressure distribution, are performed. Pressure distribution contours visually identify hull regions contributing significantly to the added resistance. Simulation results are compared to available experimental data and results based on empirical methods recommended by authorities. This study aims to establish a practical procedure for obtaining reliable added resistance coefficient in short waves.

1. Introduction

Added resistance in waves is a highly demanding research topic in marine hydrodynamics, driven by the imperative to enhance ship performance in seaways, which is now stringently regulated by the International Maritime Organization (IMO). It is acknowledged that added resistance is a derived quantity of seakeeping studies, focusing on ship motions that become significant when the wavelength is comparable to the ship's length. Consequently, efforts to improve the accuracy of added resistance calculations have been predominantly concentrated on the long wave region, where the peak of added resistance is observed. However, we must recall that the mean added resistance in seaways \bar{R}_{AW} is predicted in combination with a seaway spectrum S_f . Take a simplified case that a larger modern containership navigating in a seaway that is represented by long-crested wave, i.e.:

* Corresponding author.

E-mail address: skliu@ntu.edu.sg

$$\bar{R}_{AW}(T, H_S; U) = 2 \int_0^{\infty} \frac{R_{AW}(\omega, U)}{\zeta_A^2} S_f(\omega, H_S) d\omega \quad (1)$$

where ζ_A is wave amplitude, ω is circular frequency of waves, U is ship speed, T is wave periods, H_S is significant wave height, S_f is frequency spectrum. The full-developed seaway condition in open sea is often expressed by the two-parameter (significant wave height H_S and the mean period T_1) modified Pierson-Moskowitz spectrum as follows:

$$S(\omega) = \frac{173H_S^2}{T_1^4\omega^5} \exp\left[-\frac{691}{T_1^4\omega^4}\right] \quad (2)$$

Fig 1 illustrates the modified Pierson-Moskowitz seaway spectrum with mean centroid wave periods T_1 of 4, 6, and 8 secs and a unit significant wave height, along with the normalized added resistance of the ship in head waves. The graph clearly shows that changes in wave periods leads to different sections of the RAO to contribute to the estimation of mean added resistance. Notably, the added resistance in relatively short regular waves plays an important role in predicting the mean added resistance in seaways. This has been discussed by Steen & Faltinsen [1] and recently highlighted by Liu and Papanikolaou [2] and Liu et al. [3].

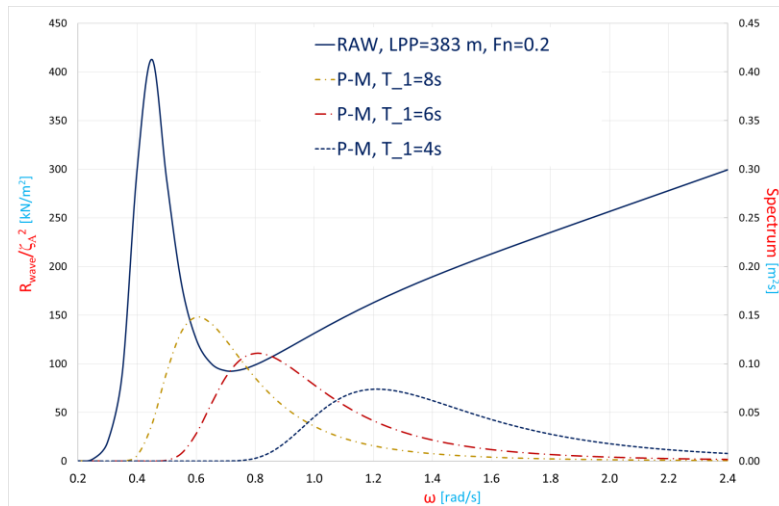


Fig. 1 Added resistance of a ship at $Fn=0.2$ in regular waves, together with three wave spectra [4]

Generally, “short wave” refers to wavelength to ship length ratio $\lambda/L < 0.5$. In such conditions, incident waves are primarily reflected, and ship motion remains minimal. As a result, the diffraction component around the ship’s bow significantly contributes to increased resistance. Unfortunately, classic potential flow theory based seakeeping models and methods fall short for predicting the added resistance in this region [5-7]. Chen [8] proposed a new formulation to address this issue. Research in this area is highly challenging due to various constraints on both experimental and numerical studies, indicating a need for significant advancements in this field. Several dedicated experimental investigations into the prediction of added resistance in short waves have been published [e.g., 9-10], which have shown the challenges in experimental studies, particularly when the wavelength-to-ship length ratio (λ/L) is less than 0.3. Sogihara et al. [11] discussed in detail the challenges related to the necessity for using larger models in conducting seakeeping tests in short waves. van Essen et al. [12] discussed the difficulty in generating stable small amplitude waves with wave makers. Additionally, the exposure time must be extended while ensuring avoiding tank wall interference [13]. Finally, the added resistance due to wave effects is relatively small compared to drag, leading to significant measurement noise [14-15]. These factors contribute to a high degree of uncertainty in short wave test results, even in head waves. Recently, ITTC has tasked the Seakeeping Committee with conducting an experimental study campaign to advance fundamental research on added resistance in waves [16].

On the other hand, continuous efforts have been devoted to the development of theoretical models over the years. Havelock [17] derived a theoretical formula to calculate the steady force acting on a fixed vertical circular cylinder in waves. Fujii and Takahashi [5] proposed a semi-empirical formula for the added resistance

due to diffraction by introducing two correction factors to Havelock's approach: one accounting for speed effects and the other for the diffraction coefficient of a thin plate [18]. Faltinsen et al. [6] developed an asymptotic formula for the added resistance on wall-sided hull forms in short waves of arbitrary direction, neglecting the influence of viscosity and sharp corners. This work can be viewed as a further development of Havelock's formula for cases involving forward speed. Fujii, in discussion with Faltinsen et al. [6], pointed out that for full ships, the results based on this formula agree well with experimental data, but for fine hull ships, there are considerable discrepancies compared to experimental data. Kwon [19] focused on the impact of short sea waves on ship speed performance. He introduced the draft correction coefficient based on the Smith effect, which states that the interaction between hull and wave exists only between the free surface and the ship bottom. Matulja et al. [20] studied added resistance in waves using Faltinsen's pressure integration, Salvesen's potential flow, and a short-wavelength empirical approximation, validating the results against experiments. Ogiwara et al. [21] confirmed the validity of this draft correction. More recently, Mourkogiannis and Liu [22] proposed a physically more robust semi-empirical formula that considers the effects of forward speed, partial reflection, finite water depth, and energy transmission below the hull.

Though these developments have contributed significantly to the creation of more simplified and transparent methods for use in regulations and industry standards [23-24], the discussion on further improving these models continues to be a focal point in ship hydrodynamics [25-29]. Given the complexity of the hydrodynamic problem at hand, it is essential to integrate the strengths of various methods to gain deeper insights. The use of computational fluid dynamics (CFD) software to simulate the phenomena in a well-controlled virtual environment is particularly valuable for enhancing our understanding of the underlying physics. For instance, Bunnik et al. [30] presented a comparative study on the prediction tools for seakeeping, where the uncertainty in predicting added resistance in short waves is highlighted. Guo et al. [14] used ISIS-CFD solver to predict the added resistance of KVLCC2 in head waves in short waves of $\lambda/L \approx 0.4$. The number of cells per wavelength and wave height were $\lambda/\Delta x > 70$ and $H/\Delta z > 11$, respectively, and the time step was $T_e/\Delta t = 140$. Lee et al. [31] used STAR-CCM+ to study the added resistance and motions of a KCS with a rudder in head waves, showing good agreement between simulations and experiments. Kobayashi et al. [32] performed a detailed parametric analysis on the added resistance and ship motions for head waves for the DTC and JBC hulls, resulting in a guideline for determining the added resistance and ship motion in head waves. One of the extensively investigated scenarios in this study concerns $\lambda/L = 0.4$, as representatives for short waves. In these studies, the time histories of added resistance are generally not published and the discussion on uncertainty in data post-processing has been rare.

In this study, numerical simulations of the added resistance acting on the KCS model in short regular head waves ($0.22 \leq \lambda/L_{pp} \leq 0.65$) are conducted using the CFD software FINETM/Marine, which solves the Unsteady Reynolds-Averaged-Navier-Stokes (URANS) equations. The simulation results are validated against experimental data available from the literature in public domain. The added resistance is systematically investigated for different short wavelengths at two ship speeds, corresponding to Froude numbers $Fn = 0.15$ and $Fn = 0.26$. The wave generation observed wave pattern around the ship, hydrodynamic pressure distribution, time history of the ship's resistance in waves, and residuals are presented and discussed in detail. In order to remove numerical noise, Fast Fourier Transform (FFT) is applied to analyse the selected non-dimensional longitudinal force signals in regular head waves to derive the mean value of the added resistance. As such, we highlight uncertainties at every step of the simulation and analysis. Possible measures to reduce these uncertainties have been implemented. This study aims to provide insights for establishing guidelines for obtaining reliable added resistance coefficient in relatively short waves.

2. Ship geometry and testing conditions

The KCS containership design used in the Tokyo CFD Workshop (2015) is scaled down to 1:31.6 for CFD calculations. The model does not include a rudder or propeller. Table 1 provides the specifications of the scaled model, including the main particulars and parameters. The study involves the simulation of two separate scenarios:

1. Resistance in calm water at two different speeds, corresponding to Froude numbers $Fn=0.15$ and 0.26 , and the ship is free to trim and sink. $F_{x,calm}$ denotes the longitudinal force exerting on the model in calm water.
2. Resistance in waves: In this scenario, the ship's performance is simulated in regular head waves at two advancing speeds. The ship's initial position is set at its equilibrium state in calm water, namely, with a preset trim and sinkage. $F_{x,wave}$ denotes the longitudinal force exerting on the model in waves.

Table 1 Main Particulars of the KCS Model

Particulars		Unit	Full-scale	Model-scale
Scale		-	1	1:31.6
Length between perpendiculars	L_{PP}	m	230	7.2786
Length of waterline	L_{WL}	m	232.5	7.3493
Maximum beam at the waterline	B_{WL}	m	32.2	1.0189
Design draft	T	m	10.8	0.3418
Depth	D	m	19.0	0.6013
Displacement	∇	m ³	52061.7	1.6454
Block coefficient	C_B	-	0.6505	0.6505
Midship section coefficient	C_M	-	0.9849	0.9849
Center of gravity, longitudinal	L_{CG}	m	111.6	3.4940
Center of gravity, vertical	V_{CG}	m	14.3	0.4525
Radius of gyration y and z direction	K_{YY}, K_{ZZ}	m	57.5	1.8200
Momentum of inertia y and z direction	I_{YY}, I_{ZZ}	m ⁴	1149782	1.1530
Ship velocity	u ($Fn=0.15/0.26$)	m/s	7.20/12.35	1.2810/2.1960

Table 2 displays the simulation matrix. Two ship speeds are involved, corresponding to Froude numbers $Fn=0.15$ and $Fn=0.26$, respectively. Four wavelengths are concerned, corresponding to wavelength-to-ship length ratios λ/L_{PP} of 0.22, 0.33, 0.40 and 0.50, respectively. The wave height-to-wavelength ratio is set as $H/\lambda=1/30$, in line with ITTC recommendation [33]. Finally, a case with $\lambda/L_{PP}=0.65$, $H/\lambda=1/60$, $Fn=0.26$, where experimental results is available [34], is included for validation purposes. General study of the added resistance in waves of $\lambda/L_{PP}>0.50$ has been completed in an earlier study [35].

Table 2 Matrix for CFD simulations, model-scale

Case No	Fn	Wavelength/ship length (λ/L_{PP})	Wave height H (m)	Wave steepness (H/λ)	Encounter period T_e (s)	Motion	
1	0.15	Calm Water					
2	0.26						
3	0.15	0.22	0.054	1/30	0.56	Constrained	
4		0.33	0.080		0.75	Constrained	
5		0.40	0.097		0.85	Constrained	
6		0.50	0.121		0.99	Constrained	
7	0.26	0.22	0.054	1/30	0.43	Constrained	
8		0.33	0.080		0.58	Constrained	
9		0.40	0.097		0.67	Constrained	
10		0.50	0.121		0.79	Constrained	
11	0.26	0.50	0.121	1/30	0.79	Free	
12	0.26	0.65	0.079	1/60	0.96	Free	

3. Numerical methodology

3.1 Numerical modelling

The FINETM/Marine software used in this work has the Equipe Modélisation Numérique (EMN) ISIS-CFD solver in its core. The simulation solves the 3D unsteady RANS equations, employing the two-equation $k-\omega$ SST turbulence model. The software is capable of handling multiphase flows and dynamic grids. Temporal discretization is achieved using a fourth-order implicit scheme, while velocity and pressure coupling is resolved through the Semi-Implicit Method for Pressure-Linked Equations (SIMPLE). The ship's motion is modelled with an analytic weighting mesh deformation approach, and the free surface is captured using a Volume of Fluid (VoF) approach.

3.2 Computational domain and boundary conditions

The computational domain dimensions are defined relative to the ship's size and wavelength, with the reference length set as $L_{ref} = \max(L_{PP}, \lambda)$. To minimize computational effort, only half of the hull geometry is considered for the resistance simulation. The domain spans $-4.0L_{ref} < x < (L_{PP} + 1.5L_{ref})$, $0.0 < y < 2.0L_{ref}$, and $-4.0L_{ref} < z < 2.0L_{ref}$. Fig 2 illustrates half of the computational domain along with the applied boundary conditions for the simulation.

A symmetry boundary condition is imposed along the centerline plane. The top and bottom surfaces are assigned updated hydrostatic pressure conditions, while the far-field is defined at the outlet boundary. For calm water simulations, a far-field condition is applied at the inlet, whereas wave simulations utilize a wave generator at the inlet. No damping zone is used in calm water simulations; however, for regular head wave cases, a damping zone is implemented at the outlet to prevent wave reflections.

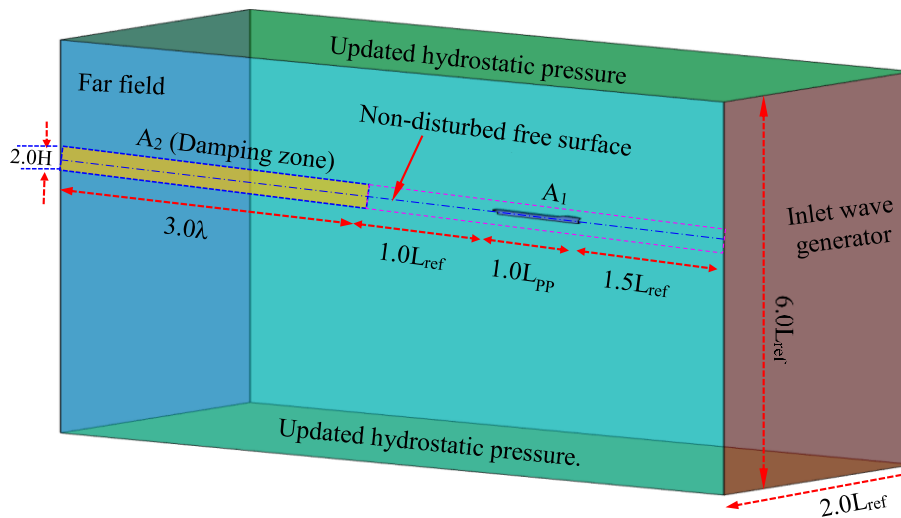


Fig. 2 Computational domain and boundary conditions applied in the seakeeping simulations.

3.3 Mesh generation

The mesh is generated using FINETM/Marine HEXPRESS through a five-step procedure: initial mesh creation, geometry adaptation, snapping to the geometry, optimization, and the finally of viscous layers. Local refinement is applied to accurately capture the free surface and the complex flow around the hull, while the mesh becomes progressively coarser toward the top and bottom of the domain. A boundary layer mesh, also known as the viscous layer mesh, is applied on the hull surface to accurately predict wall shear stress within the wall function framework. Twenty prism layers are incorporated around the hull, with the initial layer height set to 6.342×10^{-4} m corresponding to a target Y^+ value of approximately 30 for model-scale simulations. An inflation method ensures a smooth transition between the viscous inner mesh and the coarser outer Eulerian

mesh. The ship's speed is used as a reference when defining the viscous layers. Fig 3 presents the Y^+ distribution on the hull surface, showing that most of the hull falls within the desired range of 20-30, ensuring good boundary layer resolution. The variation of Y^+ from bow to stern indicates that local flow conditions influence Y^+ . Overall, the Y^+ values are within an acceptable range, ensuring a satisfactory capture of near-wall phenomena for the model-scale simulation.

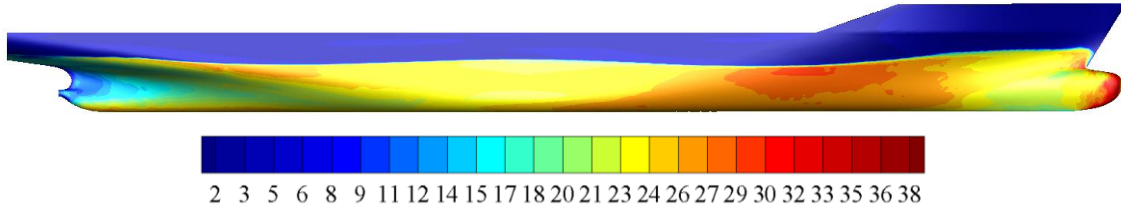


Fig. 3 Side view of the Y^+ value distribution on the surface of the ship advancing in calm water

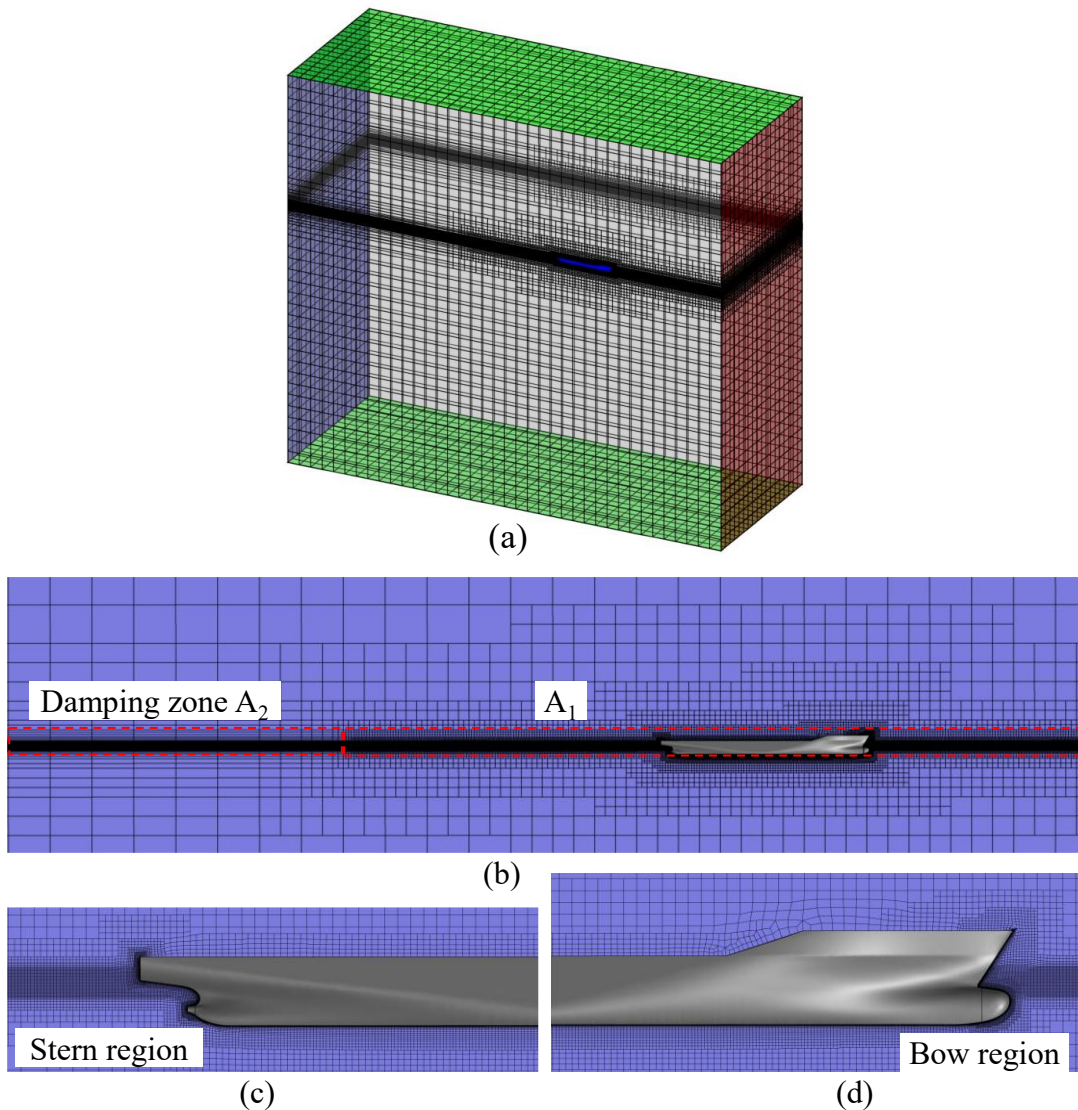


Fig. 4 Grid generation for the seakeeping simulations

Fig 4(a) shows the mesh distribution in the computational domain. As shown in Fig 4(b), the free surface refinement is achieved using two distinct refinement boxes. The first refinement box, A_1 , spans from the inlet boundary to a distance of $1.0L_{ref}$ behind the ship, while the second refinement box expands from $1.0L_{ref}$ behind the ship to the outlet. Within box A_1 , the number of cells per wavelength in the x -direction is $\lambda/\Delta x=70$. In the y -direction, the cell size (Δy) per wavelength is set to $4 \times \Delta x$. The discretization in the z -direction is defined as

$H/\Delta z = 20$, where H represents the wave height. The second refinement box, known as A2, is a damping zone designed to reduce the reflection interference and to limit the size of the computational domain and to reduce the overall CPU cost. In the x -direction, the cell size (Δx) per wavelength is set to 48 times Δx , while in the y -direction, the cell size (Δy) per wavelength is set to four times Δy . The discretization in the z -direction, however, remains consistent with the parameters used in the first refinement box (A_1), with $\Delta z = H/20$. The discretization scheme fully satisfies the recommendations of ITTC [35]; it also exceeds the requirements recommended by Guo et al., [14] and Kobayashi et al. [32], where satisfactory results were obtained for short waves. This ensures the mesh resolution is fine enough to accurately capture the free surface dynamics and the interaction between the ship and the water. The resultant computation grid ranges from 7 million to 9.6 million, depending on the wavelength.

According to the ITTC procedure [35], simulations employing one or two-equation turbulence models should utilize at least 100 time-steps per wave period or ensure that the time step Δt is smaller than 0.01 times the ship's length (L_{PP}) divided by the ship's velocity (U_{ship}) or $0.01 L_{PP}/U$. In addition, in the work of Guo et al., [14] the time step was $T_e/\Delta t=140$ and in the work of Kobayashi et al. [32] the time step was $T_e/\Delta t=48$. Considering all the evidence, in the current simulations particularly for short wavelengths, (110-150) time-steps per encounter period are employed.

3.4 Added Resistance Coefficient in Waves

We are interested in the added resistance due to waves R_{AW} , which can be computed by subtracting the total force in calm water $F_{x,calm}$ from the total force in waves $F_{x,wave}$ as follows:

$$R_{AW} = -(F_{x,wave} - F_{x,calm}) \quad (3)$$

After obtaining the time history of R_{AW} , FFT is applied to transform a time-domain signal into its frequency components. The mathematical model of FFT can be described as follows:

$$X(k) = \sum_{j=0}^{N-1} [R_{AW}/(\rho g A^2 B^2 / L_{PP})] e^{-j \frac{2\pi n k}{N}} \quad (4)$$

where:

- $A=H/2$ is incident wave amplitude and ρ is water density in kg/m^3 .
- N is the number of sampling points in the FFT analysis.
- k is the index of the frequency component, ranging from 0 to $N-1$, where '0' represents the zeroth order frequency.
- $X(k)$ is the output in the frequency domain, representing the magnitude of the frequency component indexed by k .
- The zero-frequency component corresponds to added resistance coefficient, $C_{AW} = X(0)$.

In this study, the Fast Fourier Transform (FFT) is used in MATLAB (<https://www.mathworks.com/help/matlab/ref/fft.html>) on to analyze the frequency components of the data. The FFT effectively converts data from the time domain to the frequency domain, helping signal processing and analysis. The built-in FFT functions in MATLAB minimize the computational cost, allowing for the handling of large datasets with high precision. This technique allows for the identification of dominant frequencies, and spectrum analysis, which improves the understanding of simulation findings.

4. Numerical results and discussions

4.1 Wave generation

In the present study, the Second-order Stokes waves are implemented to represent the incoming regular wave [37]. This section examines the quality of the generated waves for various wavelength-to-ship length ratios and wave steepness conditions. Fig 5 illustrates the top view of the computation domain with the locations of four probes distributed on the free surface, marked by the red circular points, namely P_1 , P_2 , P_3 , and P_4 , respectively. Specifically, P_1 is in front of the ship, while P_2 and P_3 indicate the ship's mid and stern

positions, respectively. P_4 is a point located behind the stern. In the simulations, the profile of regular waves propagating in the negative x -axis is tracked.

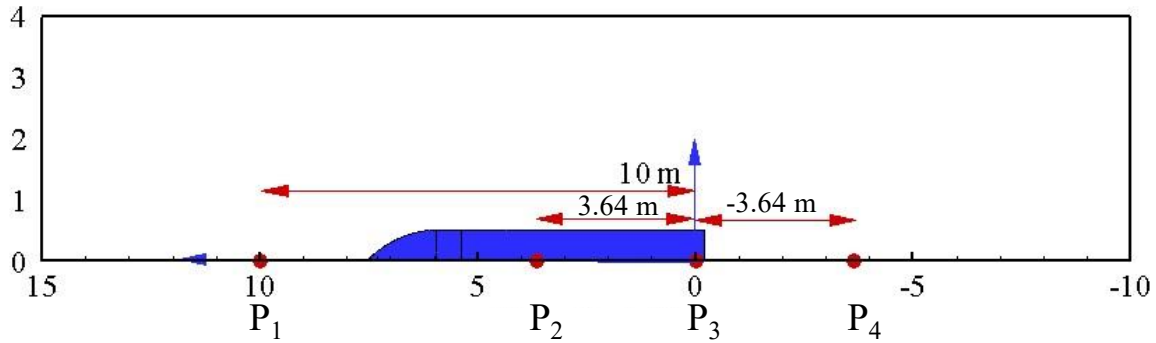


Fig. 5 Locations of 4 probes

Figs 6-9 presents the simulated free surface profiles as monitored by each of the probes for different wavelengths. Fig. 6 shows that the stable wave profile observed at P_3 for the case of $\lambda/L_{PP}= 0.50$ is in between $t/T=20-35$. Fig. 7 shows that the stable wave profile observed at P_3 for the case of $\lambda/L_{PP}= 0.40$ is approximately after $t/T=23$. Fig. 8 shows that the stable wave profile observed at P_3 for the case of $\lambda/L_{PP}= 0.33$ is approximately after $t/T=27$. Fig. 9 shows that the stable wave profile observed at P_3 for the case of $\lambda/L_{PP}= 0.22$ is approximately after $t/T=35$.

4.2 Monitored Wave Profile

Fig 10 illustrates the location of the wave probe (P) on the free surface at $(x=0.0, y=0.1509L_{PP})$. Figs. 10(b-c) displays the monitored simulated free surface profiles for various short wavelengths, with a constant wave steepness of $H/\lambda=1/30$ and at two different Froude numbers ($Fn=0.15$ and 0.26). For the cases of $\lambda/L_{PP}= 0.50$ and 0.40 , the observed free surface elevations appear to be very stable at both speeds after the ship met the fully developed wave.

For $\lambda/L_{PP}= 0.33$ at $Fn=0.15$, the observed free surface elevation is stable after $t/T_e=18$ and its amplitude start to increase after $t/T_e=40$. For $\lambda/L_{PP}= 0.33$ at $Fn=0.26$, the observed free surface elevation is stable after $t/T_e=20$ despite of some noise.

At $\lambda/L_{PP}= 0.22$ and $Fn=0.15$, a stable free surface profile is observed during a rather short period for $t/T_e = 27\sim 33$ after which it became unstable. Recalling the observation in Fig 9, it seems that there is no stable time window for this case, subsequently, the numerical analysis of this case will be very challenging. Another case requiring special attention refers to $\lambda/L_{PP}= 0.22$ at $Fn=0.26$ where the observed free surface elevation is stable for $t/T_e = 32 \sim 50$. When combined with the observation in Fig 8, the time window that can be used for further analysis is limited to $t/T_e = 40-50$. These observations are very important for determining the appropriate time window of the obtained hydrodynamic forces for further analysis.

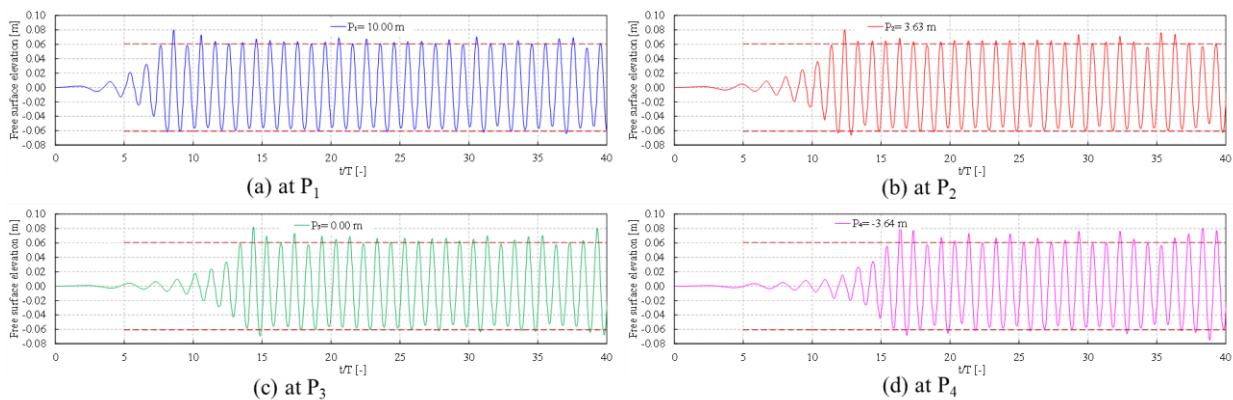


Fig. 6 Free surface elevation at different locations; wave height $H= 0.121$ m, period $T = 1.53$ s, $\lambda = 3.64$ m, $\lambda/L_{PP}= 0.50$, $H/\lambda=1/30$

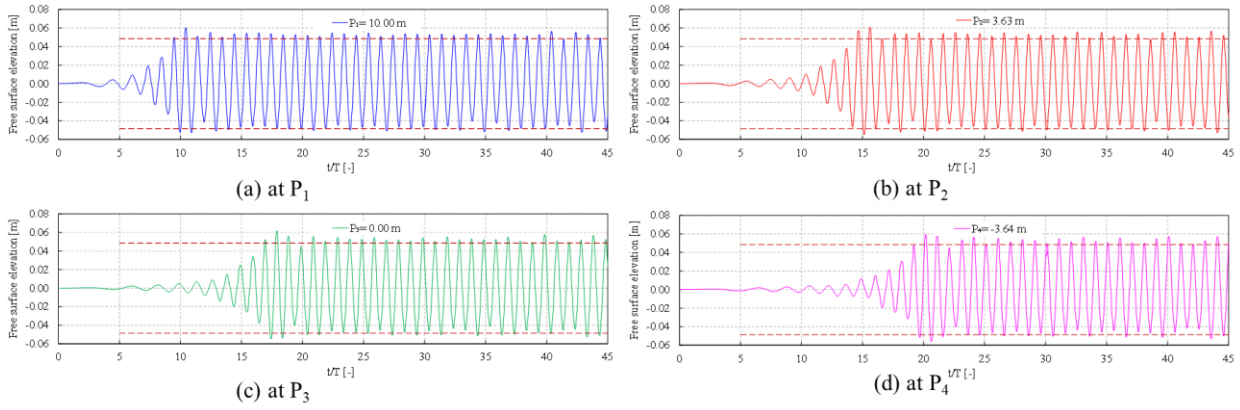


Fig. 7 Free surface elevation at different locations; wave height $H=0.097$ m, period $T=1.37$ s, $\lambda=2.91$ m, $\lambda/L_{PP}=0.40$, $H/\lambda=1/30$

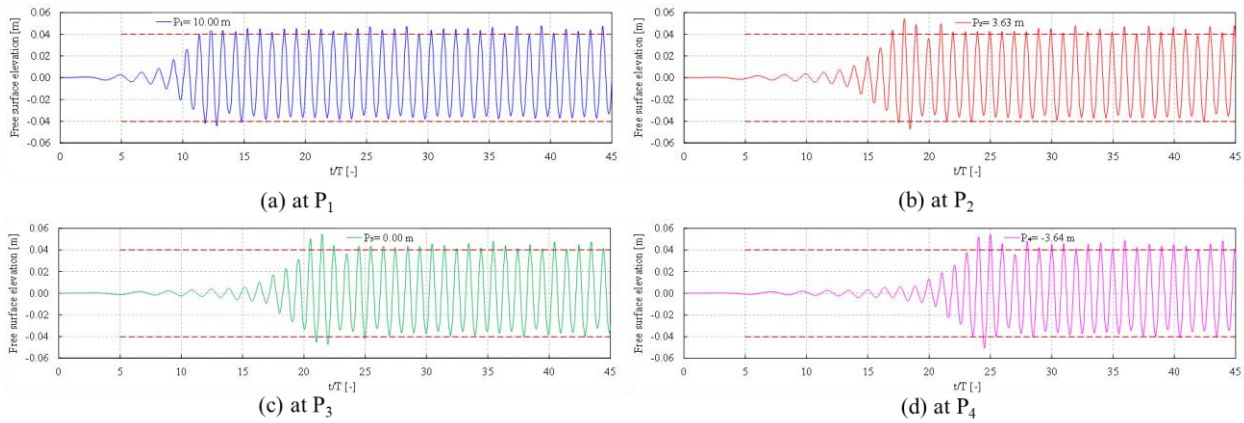


Fig. 8 Free surface elevation at different locations; $\lambda=2.41$ m, wave height $H=0.080$ m, $\lambda/L_{PP}=0.33$, period $T=1.24$ s, $H/\lambda=1/30$

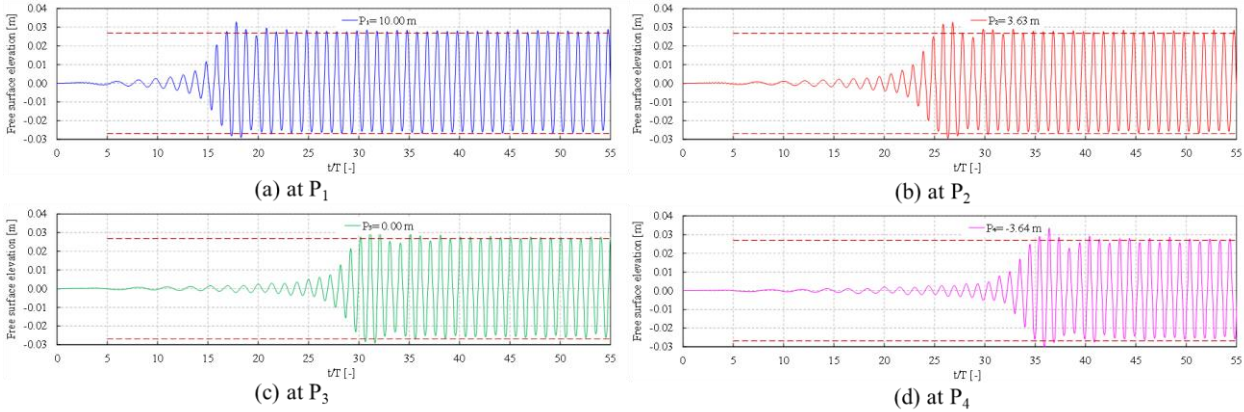


Fig. 9 Free surface elevation at different locations; $\lambda=1.61$ m, wave height $H=0.054$ m, $H/\lambda=1/30$, period $T=1.016$ s, $\lambda/L_{PP}=0.22$

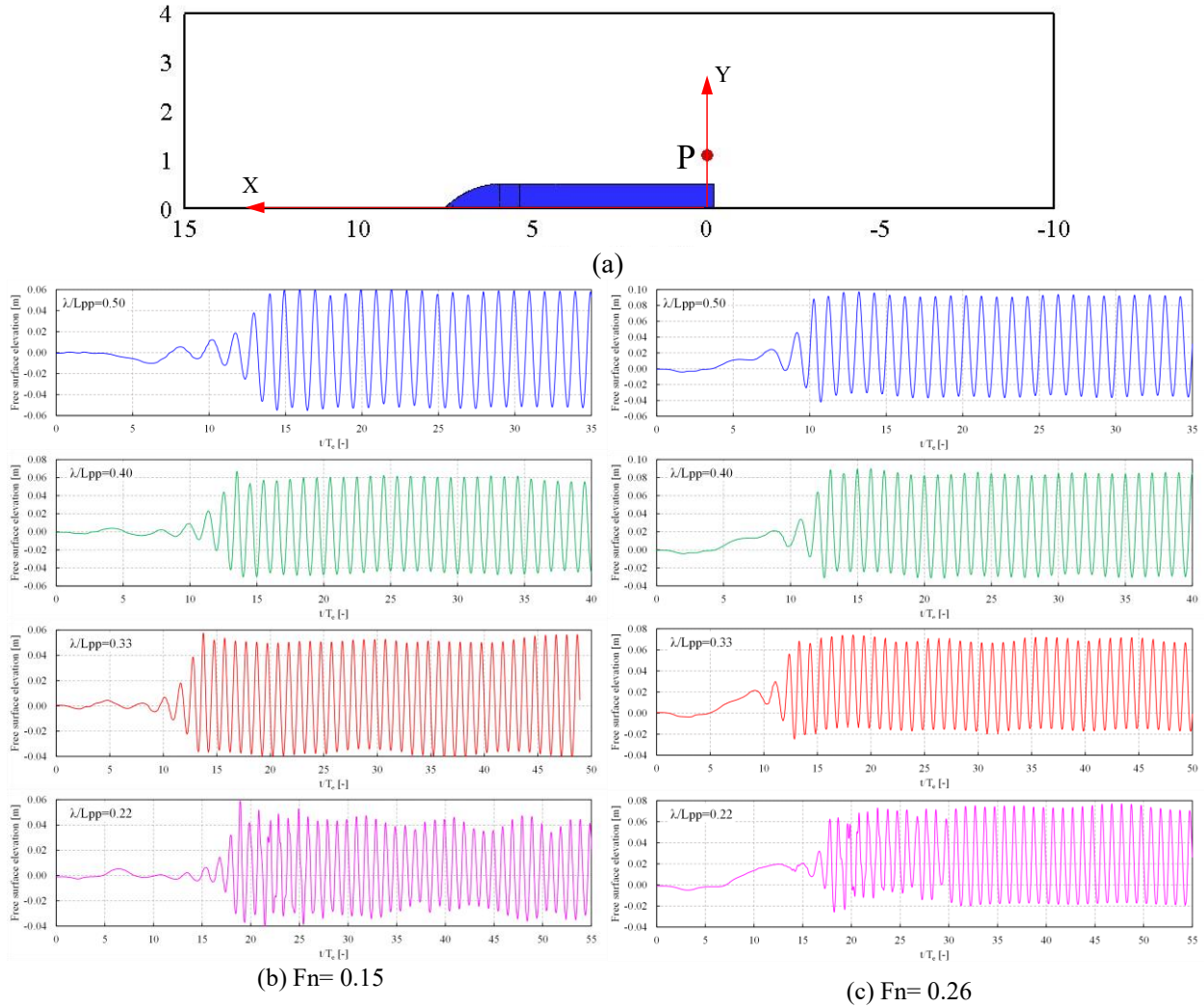


Fig. 10 Location of the wave probe on the free surface at two different Froude numbers ($F_n=0.15$ and 0.26), with a constant wave steepness of $H/\lambda=1/30$, for various short wavelengths

4.3 Validation of the simulation of ship advancing in waves

The detailed verification and validation of the simulation setup and methodology for both calm water resistance and seakeeping cases have been comprehensively addressed in a previous study [35]. While that study primarily focused on ship motion-related phenomena, this research specifically examines short-wave cases, where diffraction effects are dominant. As a further verification and validation, here we first examine the case of the KCS ship advancing in waves of length $\lambda/L_{PP}=0.65$, which is the most relevant case for the current study. Fig 11 presents the simulation results of the time series of the KCS ship's total resistance coefficient $C_T = \frac{R_T}{\frac{1}{2}\rho U_{ship}^2 A_{WS}}$, where A_{WS} denotes the wetted surface area, heave (η_3/A), and pitch (η_5/kA) motion amplitudes under the excitation of regular head waves with a wavelength-to-ship length ratio of $\lambda/L_{PP}=0.65$ over five periods of encounter. The simulation data are compared with experimental results from various institutions, including the University of Iowa (IHR), Osaka University (OU), and FORCE Technology in Denmark (FORCE) [34]. It is noted that the C_T results from FORCE exhibit highly oscillatory behavior, which is attributed to structural resonance in the rigid mount near the heave and pitch resonance conditions

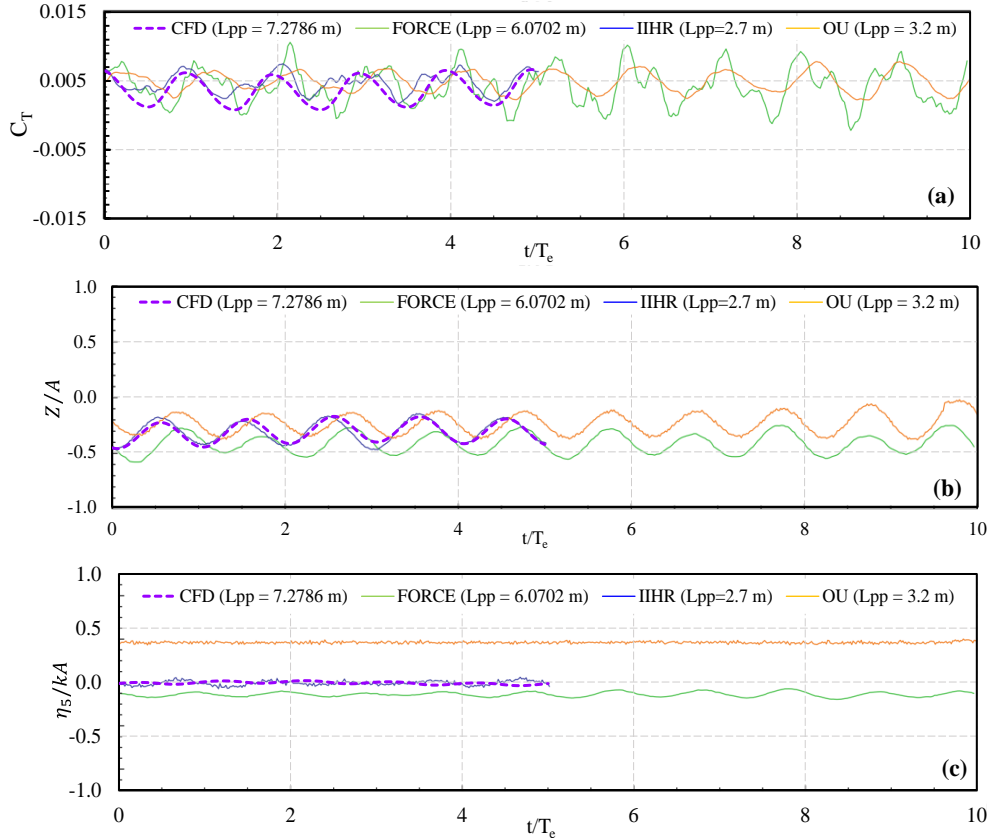


Fig. 11 Comparison of the time series of the total resistance coefficient (C_T), heave (Z/A) and pitch (η_5/kA) motions of the KCS ship in regular head waves, $\lambda/L_{PP}=0.65$, $H/\lambda=1/60$, $Fn=0.26$

For heave motion, the amplitudes of experimental results are close, but both phase and mean values are different. For pitch, the amplitudes are essentially all zero but the mean values are different. This might be due to the initial settings in the experiments. The time series of the simulation results are shifted so that the simulation result of C_T matches the positive peak of the IIHR experimental result at 0.0 s. This is a common practice in seakeeping validation studies as the timing when the generated wave meets the model is difficult to determine exactly [38]. In addition, the time lag might be a difference of inertial property between the numerical model and actual experimental models. Unfortunately, we do not have access to the primary experimental data. After this shift, the simulation results match well the EFD results. This case study demonstrates that the simulation set-up is capable of simulating the ship's performance in short waves with satisfactory accuracy. Consistent with various seakeeping studies, heave motion diminishes as the wavelength further decreases to smaller than $0.5 L_{PP}$. Therefore, in this study, we will simplify the cases of $\lambda/L_{PP} < 0.5$ by constraining the ship motions, which can reduce the associated uncertainties.

4.4 Visualization of pressure distribution

Fig 12 shows the normalized monitored incoming wave at the location $x/L_{PP}=1.04$ from AP, which is just in front of the stem, and the non-dimensional longitudinal force (F_X) for the case $\lambda/L_{PP}=0.40$, $H/\lambda=1/30$, $Fn=0.26$ over one encounter period. Fig 13(a) depicts the instantaneous free-surface elevation around the constrained ship normalized by the ship length, $\zeta^* = \zeta/L_{PP}$ while Fig 13(b) presents the hydrodynamic pressure on the hull surface, normalized by the dynamic pressure $\frac{1}{2}\rho V^2$, illustrated by six snapshots within one encounter period. These snapshots include the side and bottom views, which reveal how the wetted area and pressure distribution change over time. It is interesting to correlate the resultant force in Fig 11 with the pressure distribution in Fig 13(b). For instance, at $t=3/6 T_e$, the force has the maximum positive value. When examining the pressure distribution, we noticed that the wave crest just hits the bow of the ship. Though this creates a high pressure at the bow, the projected area in the transverse direction is very small. In fact, a

significant portion of the wetted surface of the forebody has a very low pressure, which ultimately results in the positive force due to waves.

4.5 Numerical Residual and Convergence of the Simulations

The FINETM/Marine software offers the monitoring of numerical residuals to monitor and decide whether the convergence of the simulation. Figs 14-15 depict the velocity component residual $ResU$ values alongside time history of longitudinal force (F_X) for two ship speeds with different wavelengths at constant wave steepness.

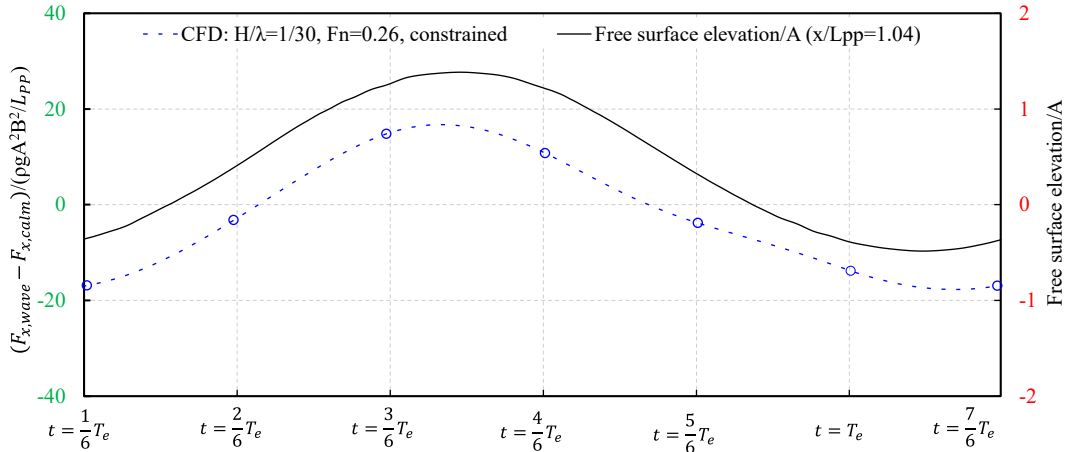


Fig. 12 Non-dimensional longitudinal force within one encounter period ($\lambda/L_{PP}=0.40$, $T_e=0.67$ s, $Fn=0.26$), together with free surface elevation recorded at $x/L_{PP}=1.04$ from AP

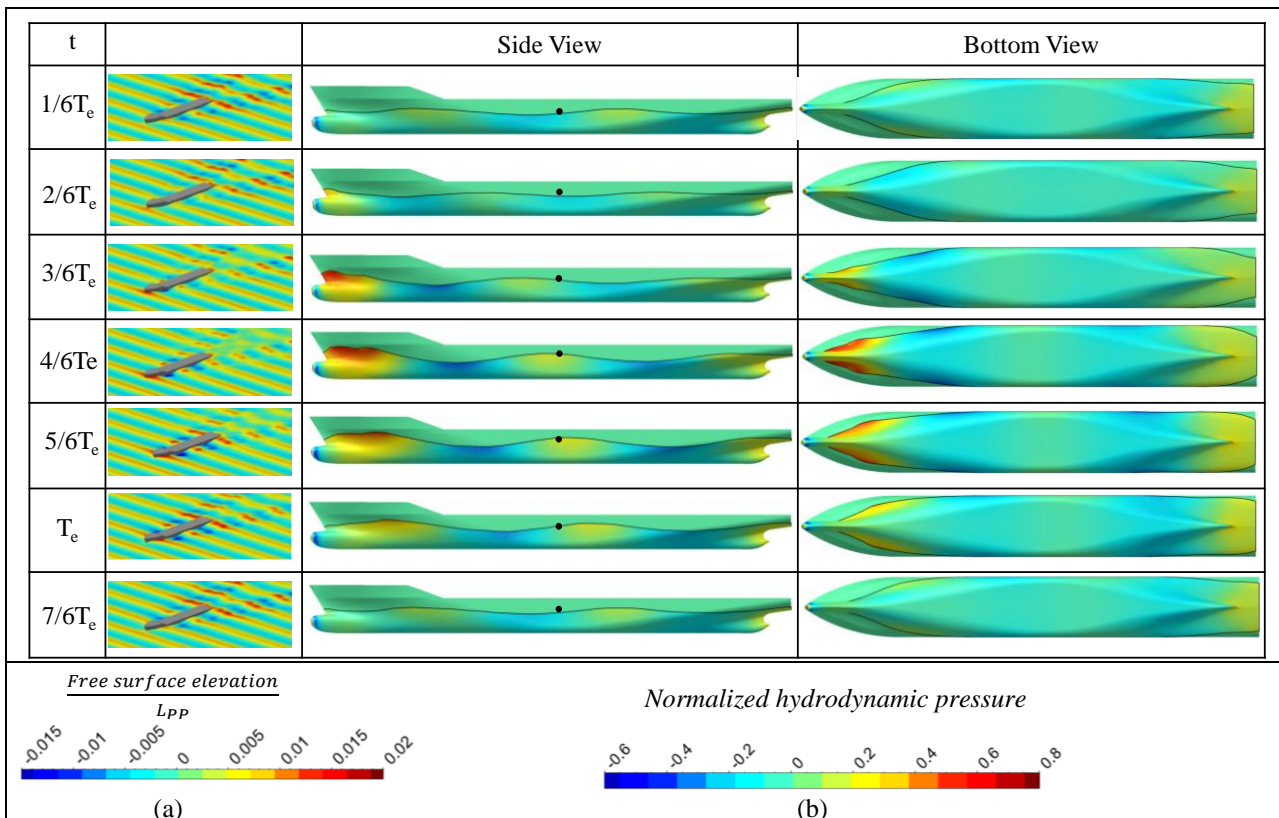


Fig. 13 Time snapshots of (a) the instantaneous relative position of ship with respect to wave (perspective view) and (b) the hydrodynamic pressure (side and bottom views) normalized by $(\frac{1}{2}\rho V^2)$, $\lambda/L_{PP}=0.40$, $H/\lambda=1/30$, $T_e=0.67$, $Fn=0.26$. The black dot denotes the center of gravity of the ship.

The x -axis indicates the number of non-linear iterations or time steps of the flow solver, while the y -axis shows the values of the residual $ResU$. As incoming waves interact with the ship, there is an increase in $ResU$ due to the transient dynamic interaction. As the transient effect dies out gradually, the residual turns to an

approximately stable value, with some minor oscillation, indicating that the simulations have converged. Subsequently, the corresponding stable region are indicated by the window in these graphs.

4.6 Determining the optimal time window

The study reveals that calculating the mean added resistance in short waves is challenging due to numerical noise, instability, and nonlinearity, as evidenced by Figs 6-10, and Figs 14-15. In steep short waves, the interaction between the hull and fluid becomes complex due to factors such as wave breaking and nonlinearity. By combining observations from these figures, the optimal time window for each case is consolidated and presented in Table 3. This recommended range is crucial for accurately and consistently predicting the mean longitudinal force (F_x). Figs 16-17 show the time windows of the simulated longitudinal force due to waves acting on the KCS ship advancing at Froude numbers (Fn) of 0.15 and 0.26, with wave steepness $H/\lambda = 1/30$ for four different wavelengths. The waves generated and measured as shown in Fig. 10 are used in these simulations. The results indicate notable differences in the behavior of the longitudinal force depending on the wavelength of the waves. At $\lambda/L_{PP} = 0.50$ and 0.40 , the longitudinal force behavior is stable, allowing for more accurate predictions of the mean longitudinal force. However, as the wavelength decreases, the nonlinearity and associated uncertainty of the longitudinal force increase. Shorter wavelength cases, such as $\lambda/L_{PP} = 0.33$ and $\lambda/L_{PP} = 0.22$, result in more unpredictable force fluctuations and significant low-frequency noise, complicating the accurate determination of the mean longitudinal force.

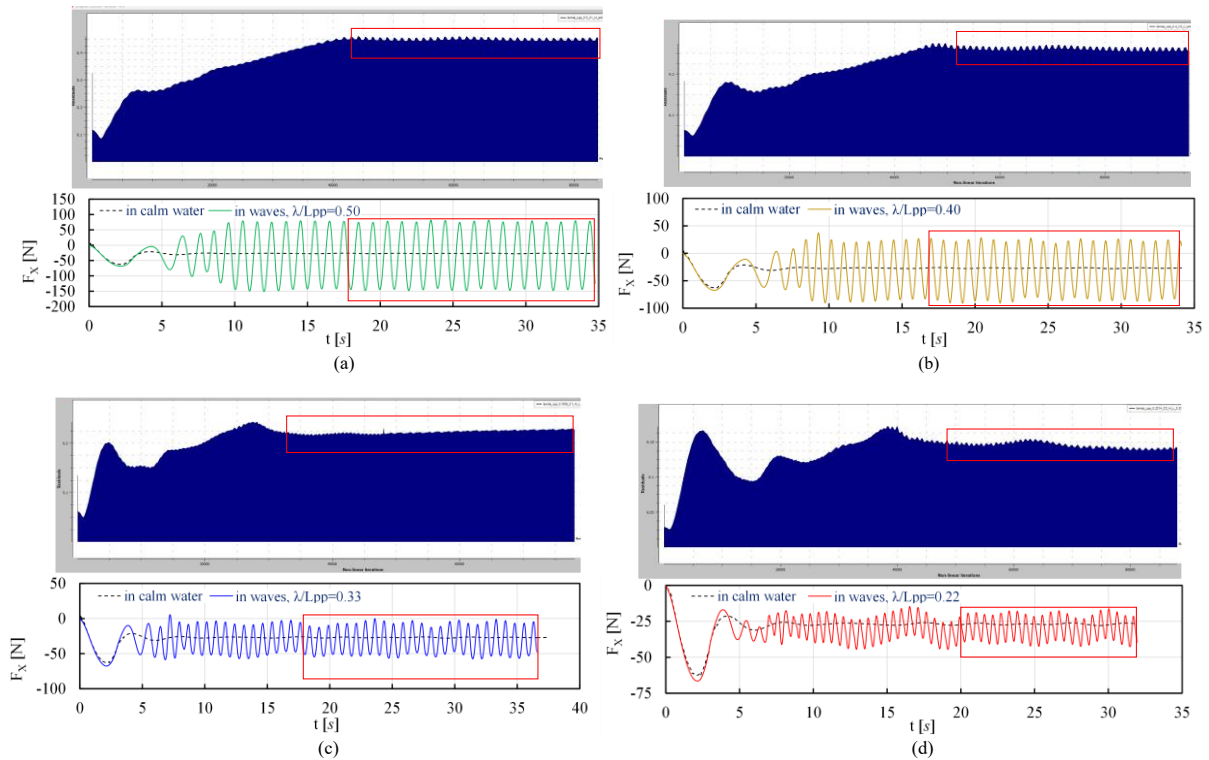


Fig. 14 Time history of longitudinal force (F_x) along with residuals, at constant wave steepness $H/\lambda=1/30$ for various short wavelengths, $Fn=0.15$: (a) $\lambda/L_{PP} = 0.50$; (b) $\lambda/L_{PP} = 0.40$; (c) $\lambda/L_{PP} = 0.33$; (d) $\lambda/L_{PP} = 0.22$.

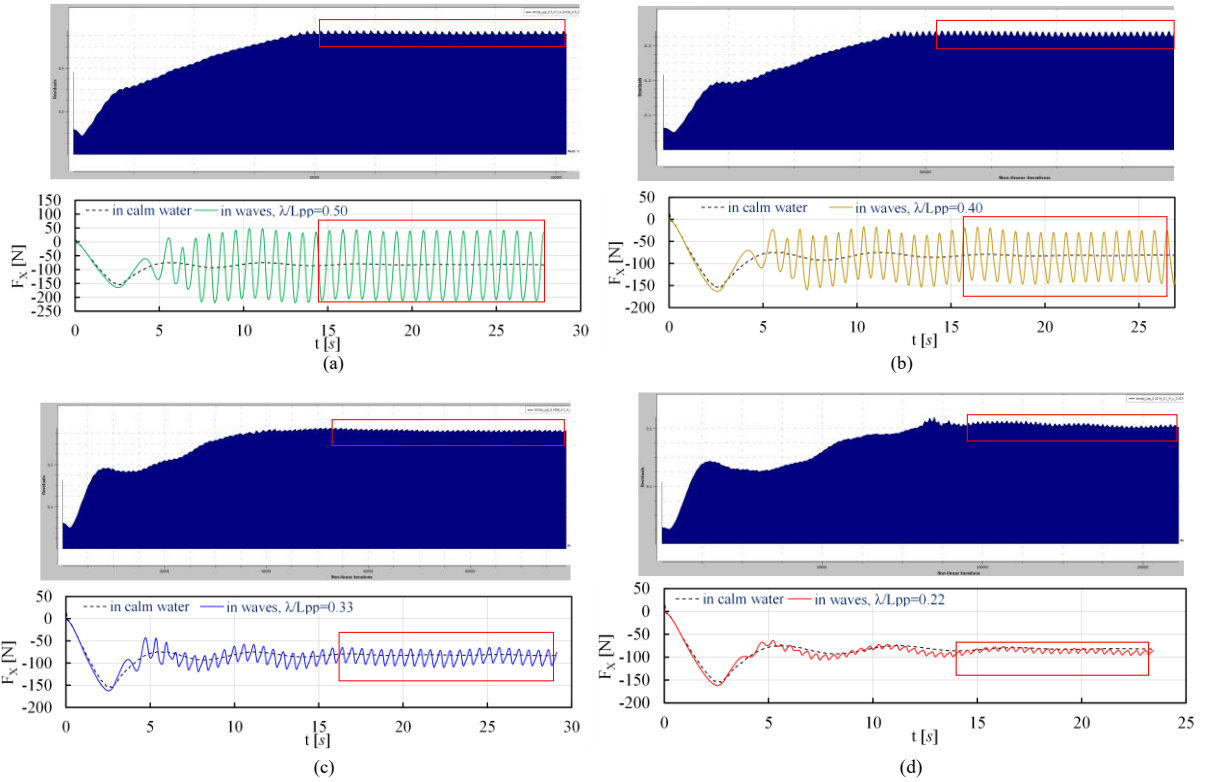


Fig. 15 Time history of longitudinal force (F_x) along with residual, at constant wave steepness $H/\lambda=1/30$ for various short wavelengths, $Fn=0.26$: (a) $\lambda/L_{pp} = 0.50$; (b) $\lambda/L_{pp} = 0.40$; (c) $\lambda/L_{pp} = 0.33$; (d) $\lambda/L_{pp} = 0.22$

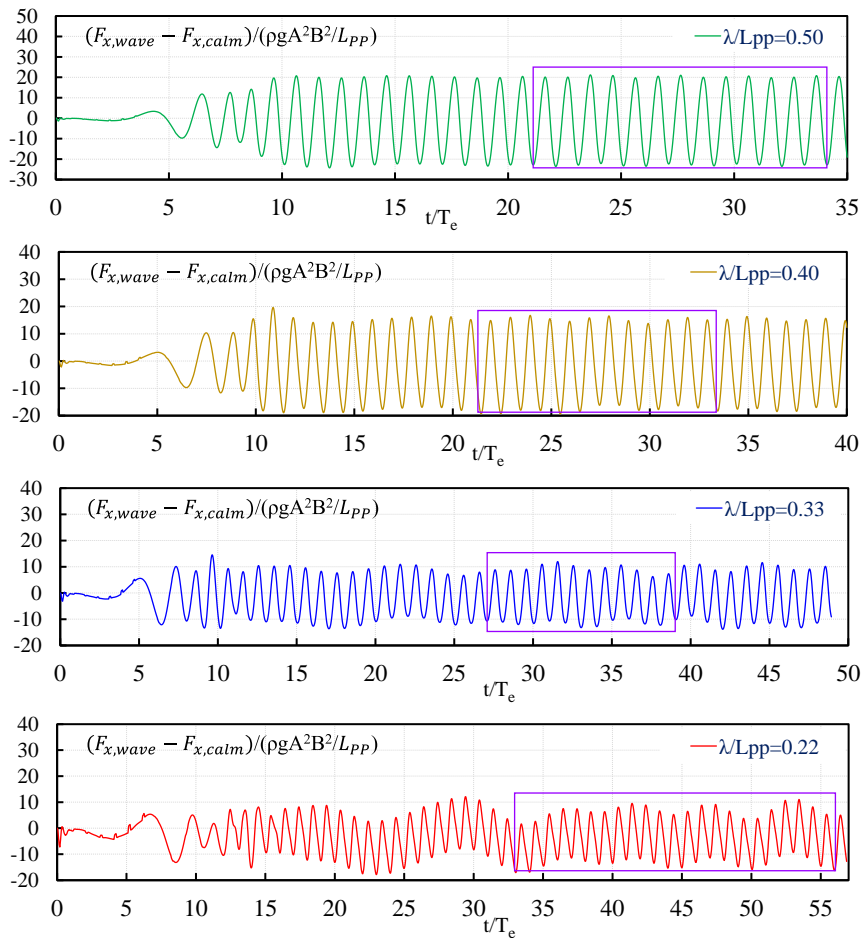


Fig. 16 Time history of the non-dimensional longitudinal force due to waves, along with the optimal time window, $H/\lambda=1/30$, $Fn=0.15$

Table 3 Recommended time window for various cases

Cases	λ/L_{PP}	Optimal Time Window as a function of t/T_e
$Fn = 0.15$	0.50	21~34
	0.40	21~34
	0.33	27~39
	0.22	36~50
$Fn = 0.26$	0.50	20~33
	0.40	24~39
	0.33	27~45
	0.22	35~49

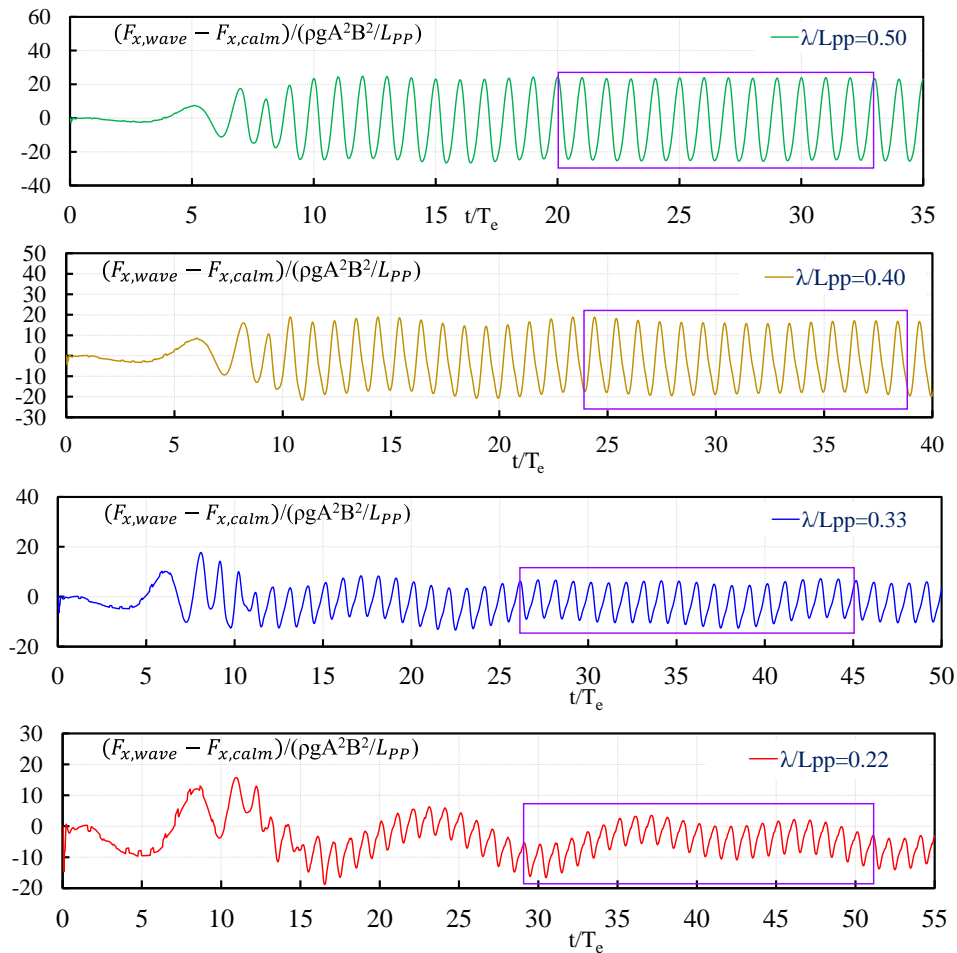


Fig. 17 Time history of the non-dimensional longitudinal force due to waves, along with the optimal time window, $H/\lambda=1/30, Fn=0.26$

4.7 Analysis of the time histories of force due to waves

To obtain the added resistance coefficient, we apply the Fast Fourier Transform (FFT) to analyze the time histories of the force in the determined optimal time window. Generally, the numerical accuracy can be improved when the data of a greater number of wave cycles is used. According to the ITTC guidelines [39], at least 10 periods of encounter are required. This section aims to check the error/uncertainty related to the sampling interval in deriving the added resistance coefficient.

Fig 18 presents the result of the FFT analysis of the force signal at $\lambda/L_{PP} = 0.40$ and $Fn = 0.26$ using the data of 5, 10, and 15 encounter periods, respectively. The y-axis represents the amplitudes and phase angle of each component, while the x-axis represents the non-dimensional frequency (f/f_e). f represents the frequency in (s^{-1}) of each component derived from the force signal and f_e refers to the encounter frequency of that case.

f/f_e indicates the normalized frequency. $\frac{(F_{X,wave}-F_{X,calm})}{\frac{\rho g A^2 B^2}{L_{PP}}}$ represents the non-dimensional amplitudes of the resistance component derived from the force signal. The left plot shows the amplitude spectrum of the longitudinal force F_x against the normalized frequency f/f_e . The red circle highlights the zero-frequency component, corresponding to the added resistance coefficient, which remained almost constant when changing the number of encounter periods. The right plot displays the phase angle spectrum (in radians) versus the normalized frequency f/f_e , showing the phase angle for each frequency. Together, these plots provide a comprehensive view of the signal's amplitude and phase across its frequency range.

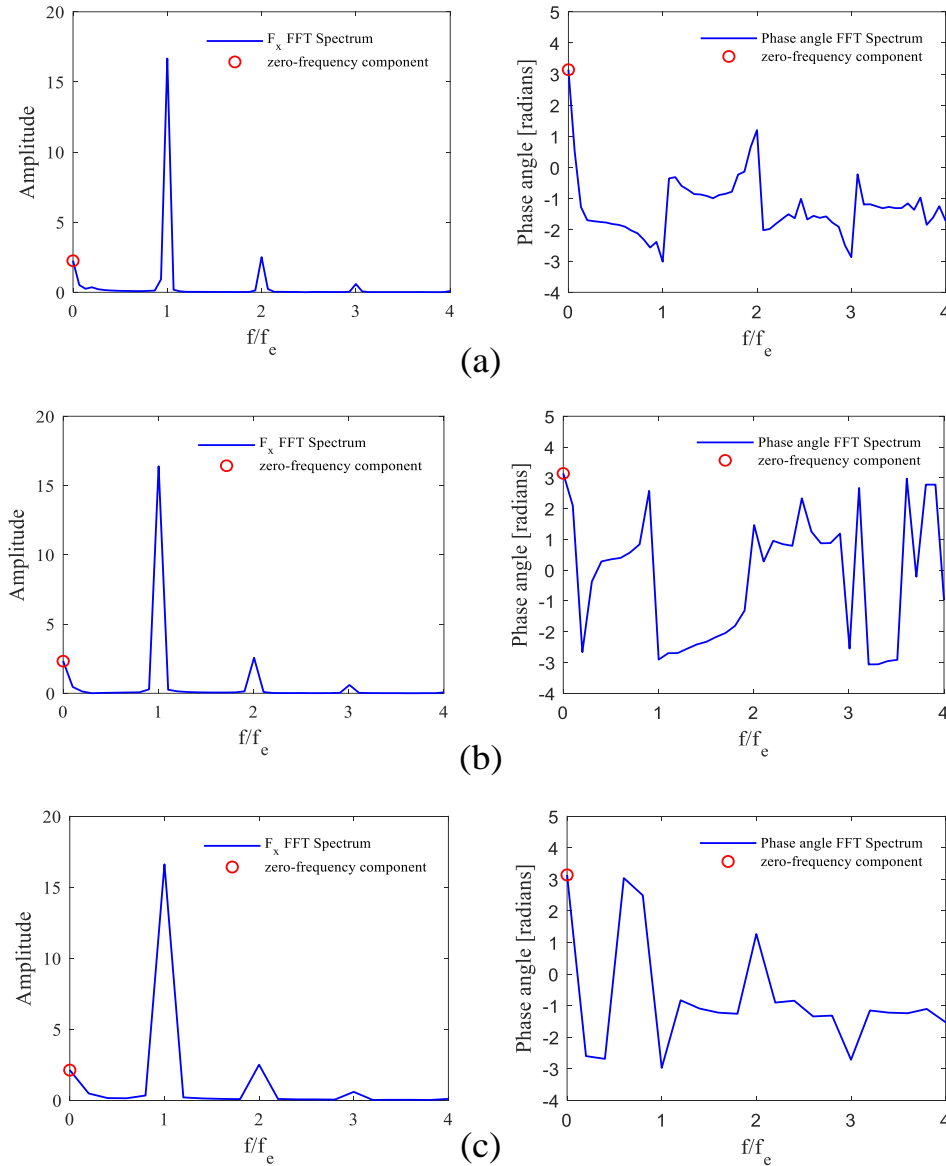


Fig. 18 FFT analysis results using the data of (a)15, (b)10 and (c)5 encounter periods, respectively. $\lambda/L_{PP}=0.40, Fn=0.26$

Figs 19-20 presents the results of FFT analysis of the force signals of the cases $\lambda/L_{PP}=0.22, Fn = 0.15$ and 0.26 , respectively. As shown in the graphs, strong lower-frequency components are present in these two very short-wave cases ($\lambda/L_{PP}=0.22$). The FFT analysis reveals significant changes in the amplitudes of the various components when the time interval, namely the number of encounter periods, varies. These findings underscore the need to use as many encounter periods as possible in seakeeping studies to ensure accurate and consistent predictions of the mean longitudinal force across various wave conditions and ship speeds. Additionally, the selection of an appropriate time window is crucial when applying FFT, as it is difficult to obtain reliable results when the force signal is contaminated by low-frequency components. More advanced numerical techniques are required to make substantial progress in this area.

The FFT analysis results for other cases are presented in the Appendix.

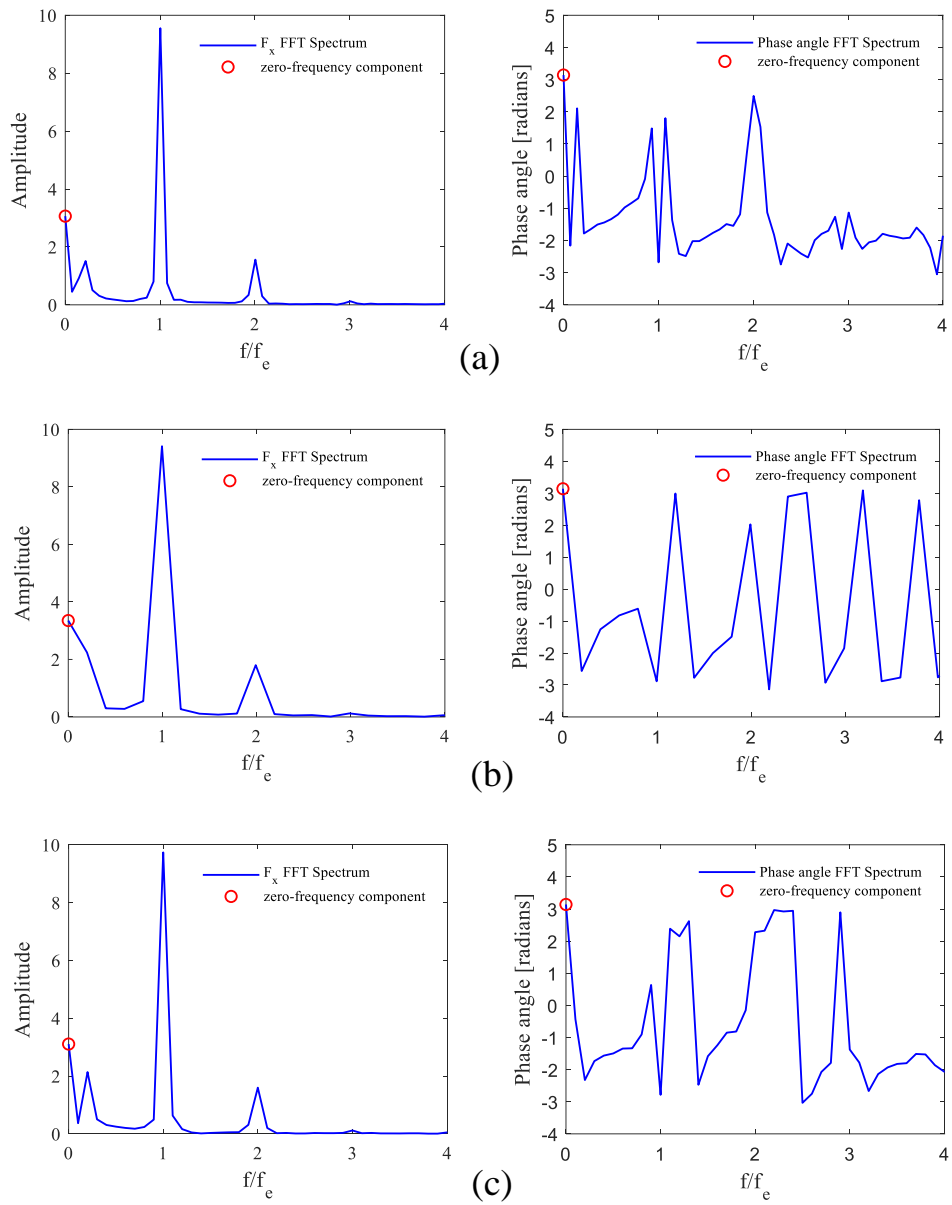


Fig. 19 FFT analysis results using the data of (a) 14, (b) 10 and (c) 5 encounter periods, respectively. $\lambda/L_{pp}=0.22$, $Fn=0.15$

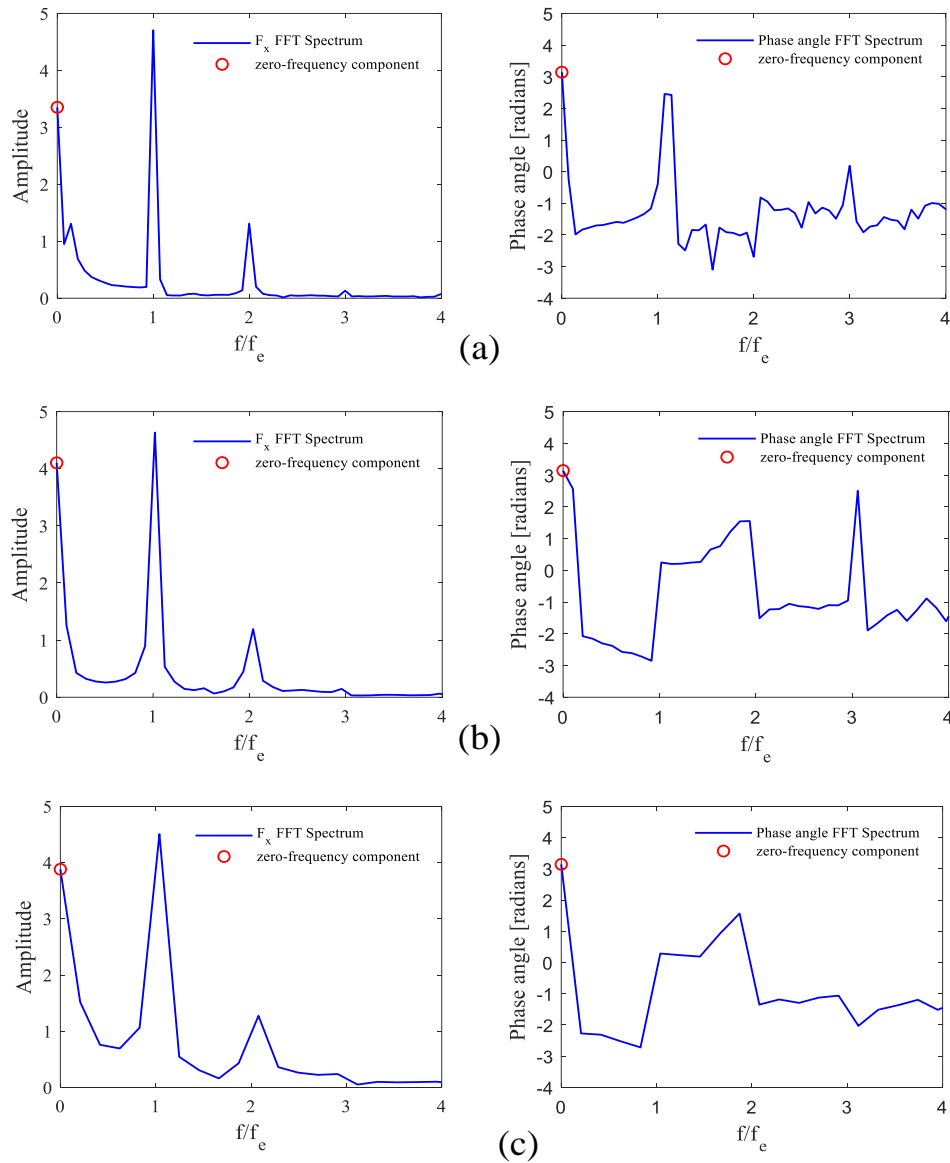


Fig. 20 FFT analysis results using the data of (a) 14, (b) 10, and (c) 5 encounter periods, respectively. $\lambda/L_{PP}=0.22$, $Fn=0.26$

4.8 Obtained added resistance coefficient

Fig 21 presents the dependence of the added resistance coefficient (C_{AW}) on the number of encounter periods at (a) $Fn=0.15$ and (b) $Fn=0.26$, respectively. The applied range of time interval mostly follows Table 3, except for $\lambda/L_{PP}=0.22$. In general, it is observed that the results obtained using data for 5 periods of encounter are not yet stable. The results obtained using data of 10 periods of encounter are very close to those obtained using data of 15 periods of encounter. The only exceptions being the two cases of $\lambda/L_{PP}=0.22$. Due to the strong lower-frequency components presented in the force signals, as shown in Figs. 16 and 17, a broader time interval that cover at least one full period of that corresponding low-frequency component is used to derive the result of the mean added resistance coefficient. As documented in ITTC procedure [36] “Analysis Procedure for Model Tests in Regular Waves”, “it is recommended to examine the time histories of all the signals. If a signal contains an exceptionally high noise level, it may require special treatment.” This is especially necessary for responses with long period.

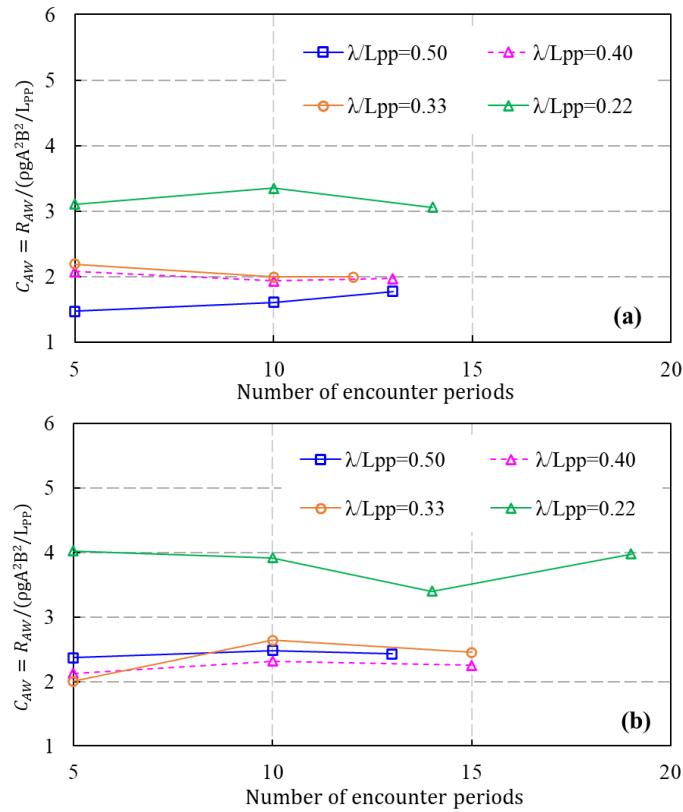


Fig. 21 Convergence study of added resistance coefficient: (a) $Fn=0.15$, and (b) $Fn=0.26$

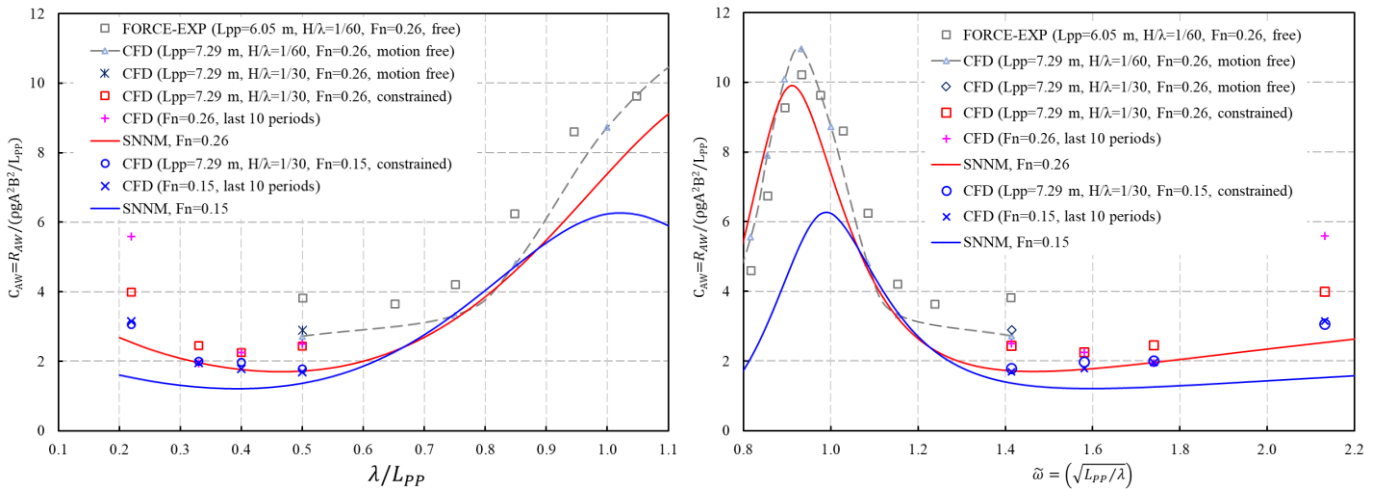


Fig. 22 Predicted added resistance coefficient in regular head waves, against either λ/L_{PP} or $\tilde{\omega} = \sqrt{L_{PP}/\lambda}$

Based on the above analysis, the added resistance coefficients of the KCS ship in regular head waves with wave steepness $H/\lambda = 1/30$ at two speeds corresponding to $Fn = 0.15$ and 0.26 are obtained and presented as a function of either λ/L_{PP} or the non-dimensional wave frequency $\tilde{\omega} = \sqrt{L_{PP}/\lambda}$ in Fig. 22. Note that, these results are aligned with those shown in Fig 21, using as much as possible data for each case to ensure high accuracy and reliability in the results, thereby reducing potential errors that might arise from insufficient sampling. Key observations include: 1) At $\lambda/L_{PP}=0.50$, the added resistance coefficients obtained from motion-free and motion-constrained simulations show slight deviations. This is reasonable due to the interaction effect between radiation and diffraction. 2) Examining the overall trend of the obtained added resistance in short waves due to the diffraction (motion-constrained), we observe that the added resistance coefficient increases linearly with the increase of wave frequency. This observation aligns with the asymptotic theory of Faltinsen et al. [6]. A similar trend has been observed in previous studies, for instance, as in Bunnik et al. [30]. Additionally, it is also noted that the gradient of the added resistance increases with the ship's speed. 3) The

results using data in the last 10 periods of encounter following ITTC guidelines [39] are also presented for reference. It is observed that for $Fn=0.26$ these results deviate significantly from the results following the recommended practice, particularly in very short waves. The observed trend does not follow the asymptotic theory of Faltinsen et al. [6]. The deviation is less significant for $Fn=0.15$. 4) the results by the empirical SNNM method, as recommended by ITTC [24] and ISO15016 [40], are also included. The CFD simulation results are close to those authoritative results, despite of some deviations. It is highlighted that the experimental results in short waves have significant uncertainty, especially in short waves. ITTC has acknowledged this issue and has been attempting to address it within the Seakeeping Committee during its 30th term [16]. The current study is partially to support to reduce the uncertainties in numerical simulations by establishing a reliable procedure. More simulations are planned to provide additional evidence to clarify these points.

5. Conclusions

In this study, the added resistance of the KCS ship due to diffraction is simulated using FINETM/Marine software, which solves the unsteady RANS equations, with the $k-\omega$ SST turbulence model. Numerical analysis is performed for different short wavelengths ($0.22 \leq \lambda/L_{PP} \leq 0.65$) at two ship speeds, and their performance characteristics are compared with available experimental results available in the open literature. This detailed analysis contributes to a more comprehensive understanding of the ship's added resistance in short regular head waves. Based on the study, the conclusions drawn are summarized below:

- The quality of the generated waves, with or without the presence of the model, are examined. Results show that the generation of stable long-time regular waves is challenging.
- Simulation results of the time histories of motion and total resistance at $\lambda/L_{PP}=0.65$ are compared to available experimental results and show good agreement.
- Snapshots of the hydrodynamic pressure distribution on the hull surface during one encounter period indicate the source of the added resistance. The study shows that the positive force observed at $t=3/6T_e$ is due to the wave crest hitting the bow, creating high pressure in a small area. Despite this, the overall low pressure on the wetted forebody surface results in a net positive force. These findings enhance our understanding of wave-induced forces on ships.
- The simulation results of the longitudinal force histories include significant low-frequency numerical noise. Using Fast Fourier Transform (FFT) on non-dimensional longitudinal force signals enables precise calculation of mean added resistance, effectively separating it from oscillatory effects and numerical noise.
- Due to the factors mentioned above in wave generation and numerical noise, obtaining a stable added resistance coefficient is challenging.
- This study contributes efficiently to advancing the understanding of added resistance in short waves. We highlight uncertainties at every step of the simulation and analysis. Possible measures to reduce these uncertainties have been implemented. It provides rich information on establishing a reliable workflow for obtaining reliable coefficients of added resistance in short waves.

Nevertheless, the findings of this research are limited by factors such as available computing resources, mesh resolution and time-step size, turbulence modelling, and other variables. For future work, we plan to explore alternative wave generation methods using FINETM/Marine software to determine if more stable waves can be produced. We will implement adaptive grid refinement to improve the accuracy of water-structure interactions in short waves. To accomplish this, future simulations will utilize high-performance computing (HPC) infrastructure, enabling the use of finer meshes and more sophisticated wave modelling within feasible computational times. In the long term, high-fidelity Direct Numerical Simulations (DNS) seem necessary for pursuing a comprehensive solution to this complex challenge. Ultimately, a deeper understanding of added resistance in waves will contribute to the development of more effective practical approaches, supporting the implementation of the IMO GHG strategy through enhanced design, operational optimization, and economic measures [41,42].

ACKNOWLEDGEMENTS

The authors are grateful to Dr GB Deng, Ecole Centrale de Nantes, for his valuable advice and discussion in conducting the CFD simulations.

This study is conducted within the project of “Prediction of the added resistance of a ship in seaways for the rational determination of installed power” financially supported by the Sembcorp Marine Lab Fund.

REFERENCES

- [1] Steen, S. Faltinsen, O.M., 1998. Added resistance of a ship moving in small sea states. Proceedings of PRADS' 98, September, The Hague, Netherlands, 521-526. [https://doi.org/10.1016/S0928-2009\(98\)80193-5](https://doi.org/10.1016/S0928-2009(98)80193-5)
- [2] Liu, S. Papanikolaou, A., 2017. On the prediction of the added resistance of large ships in representative seaways. *Ships and Offshore Structures*, 12, 690–696. <https://doi.org/10.1080/17445302.2016.1200452>
- [3] Liu, S., Shang, B., Papanikolaou, A., 2019. On the resistance and speed loss of full type ships in a seaway. *Ship Technology Research*, 66, 161–179. <https://doi.org/10.1080/09377255.2019.1613294>
- [4] Liu, S. Papanikolaou, A., 2023. Recent progress on the transparent prediction of the added resistance and powering of a ship in waves. *Proceedings of the 8th International Symposium on Ship Operations, Management & Economics (SOME)*, 7-8 March, Athens, Greece.
- [5] Fujii, H., Takahashi T., 1975. Experimental study on the resistance increase of a ship in regular oblique waves. *Proceeding of 14th ITTC*, Ottawa, Canada, 1975, 351-360. <https://doi.org/10.2534/jjasnaoe1968.1975.132>
- [6] Faltinsen, O. M., Minsaas, K. J., Liapis, N., Skjördal, S. O., 1980. Prediction of resistance and propulsion of a ship in a seaway. *Proceedings of the 13th Symposium on Naval Hydrodynamics*, 6-10 October, Tokyo, Japan, 505-529.
- [7] Liu, S., Papanikolaou, A., 2016. Prediction of the added resistance of ships in oblique seas, *Proceedings of the 26th International Ocean and Polar Engineering Conference*, June 26-July, Rhodes, Greece.
- [8] Chen, X.B., 2024. Formulations of Added Resistances. *15th International Conference on Hydrodynamics*. 2-6 September. Rome, Italy.
- [9] Kashiwagi, M., Sugimoto, K., Ueda, T., Yamazaki, K., Arihama, K., Kimura, K., Yamashita, R., Itoh, A., Mizokami, S., 2004. An analysis system for propulsive performance in waves. *Journal of the Kansai Society of Naval Architects*, 241, 67-82.
- [10] Valanto, P., Hong, Y., 2015. Experimental investigation on ship wave added resistance in regular head, oblique, beam, and following waves. *Proceedings of the 25th International Offshore and Polar Engineering Conference*, Kona, USA, 3, 19-26.
- [11] Sogihara, N., Tsujimoto, M., Fukasawa, R., Hamada, T., 2020. Uncertainty analysis for measurement of added resistance in short regular waves: Its application and evaluation, *Ocean Engineering*, 216, 107823. <https://doi.org/10.1016/j.oceaneng.2020.107823>
- [12] van Essen, S.M., Scharnke, J., Bunnik, T., Düz, B., Bandringa, H., Hallman, R., Helder, J., 2020. Linking experimental and numerical wave modelling. *Journal of Marine Science and Engineering*. 8, 198-206. <https://doi.org/10.3390/jmse8030198>
- [13] Gerhardt, F.C., Kjellberg, M., Korkmaz, B., Ljungqvist, K., Shiri, A., 2020. Determining the EEDI Minimum Propulsion Power. *Proceedings of Influence of EEDI on Ship Design & Operation Online Conference*, Royal Institution of Naval Architects, United Kingdom, 1–15.
- [14] Guo, B., Steen, S., Deng, G., 2012. Seakeeping prediction of KVLCC2 in head waves with rans. *Applied Ocean Research*, 35, 56–67. <https://doi.org/10.1016/j.apor.2011.12.003>
- [15] Lee, J., Kim, Y., Kim, B., Gerhardt, F., 2021. Comparative study on analysis methods for added resistance of four ships in head and oblique waves. *Ocean Engineering*. 236, 109552. <https://doi.org/10.1016/j.oceaneng.2021.109552>
- [16] International Towing Tank Conference, 2021. Executive Committee: Tasks and structure of the 30th ITTC technical committees and groups.
- [17] Havelock, T.H., 1940. The Pressure of Water Waves upon a Fixed Obstacle. *Proceedings of the Royal Society of London, Series A, Mathematical and Physical Sciences*, 175(963), 409-421. <https://doi.org/10.1098/rspa.1940.0066>
- [18] Ursell, F., 1947. The Effect of a Fixed Vertical Barrier on Surface Waves in Deep Water. *Proceedings of the Cambridge Philosophical Society*. 42, 374-382. <https://doi.org/10.1017/S0305004100023604>
- [19] Kwon, Y.J., 1981. The effect of weather, particularly short sea waves, on ship speed performance. PhD thesis, *University of Newcastle upon Tyne*.
- [20] Matulja, D., Sportelli, M., Guedes Soares, C., Prpić-Oršić, J. 2011. Estimation of added resistance of a ship in regular waves. *Brodogradnja*, 62(3), 259-264.
- [21] Ogiwara, S, Yamashita, S., Mifune M., 1996. On resistance increase in waves of short wavelength. *Journal of the Kansai Society of Naval Architects*, 225, 37–45.

- [22] Mourkogiannis, D., Liu, S., 2021. Investigation of the influence of the main dimensional ratios of a ship on the added resistance and drift force in short waves. *Proceedings of the 31st International Ocean and Polar Engineering Conference*, 20-25 June, Rhodes, Greece, ISOPE-I-21-3138.
- [23] International Maritime Organization, 2021. Guidelines for Determining Minimum Propulsion Power to Maintain the Manoeuvrability of Ships in Adverse Conditions. International Maritime Organization, London. MEPC.1/Circ.850/Rev.3.
- [24] International Towing Tank Conference. 2021. Report of the specialist committee on ships in operation at sea – final report and recommendations to the 29th ITTC.
- [25] Wang, J., Bielicki, S., Kluwe, F., Orihara, H., Xin, G. Kume, K., Oh, S., Liu, S., Feng, P., 2021. Validation study on a New Semi-empirical Method for the Prediction of Added Resistance in Waves of Arbitrary Heading in Analyzing Ship Speed Trial Results. *Ocean Engineering*, 240, 109959. <https://doi.org/10.1016/j.oceaneng.2021.109959>
- [26] Lee, J., Kim, Y., 2023. Development of enhanced empirical-asymptotic approach for added resistance of ships in waves. *Ocean Engineering*, 280, 114762. <https://doi.org/10.1016/j.oceaneng.2023.114762>
- [27] Liu, S., Papanikolaou, A., 2023. Recent progress on the transparent prediction of the added resistance and powering of a ship in waves. *Proceedings of the 8th International Symposium on Ship Operations, Management & Economics (SOME)*, 7-8 March, Athens, Greece.
- [28] Liu, S., Papanikolaou, A., 2023. Improvement of the Prediction of the Added Resistance in Waves of Ships with Extreme Main Dimensional Ratios Through Numerical Experiments. *Ocean Engineering*. 273, 113963. <https://doi.org/10.1016/j.oceaneng.2023.113963>
- [29] Kuroda, M., Tsujimoto, M., 2023. The Wave Correction Method for Speed Trial Analysis: Simple-NMRI method. Reports of National Maritime Research Institute. https://www.nmri.go.jp/service/repository_data/PNM23230105-00.pdf
- [30] Bunnik, T.H.J., Daalen, E.F.G., van Kapsenberg, G.K., Shin, Y., Huijsmans, R.H.M., Deng, G, Delhommeau, G., Kashiwagi, M., Beck B., 2010. A comparative study on state-of-the-art prediction tools for seakeeping. *Proceedings of the 28th Symposium on Naval hydrodynamics*, 12-17 September, Pasadena, United States, 242-255.
- [31] Lee, Y.G., Kim, C., Park, J.H., Kim, H., Lee, I., Jin, B., 2019. Numerical simulations of added resistance in regular head waves on a container ship. *Brodogradnja*, 70(2), 61-86. <https://doi.org/10.21278/brod70204>
- [32] Kobayashi, H., Kume, K., Orihara, H., Ikebuchi, T., Aoki, I., Yoshida, R., Yoshida, H., Ryu, T., Arai, Y., Katagiri, K., Ikeda, S., Yamanaka, S., Akibayashi, H., Mizokami, S., 2021. Parametric study of added resistance and ship motion in head waves through RANS: Calculation guideline. *Applied Ocean Research*. 110, 102573. <https://doi.org/10.1016/j.apor.2021.102573>
- [33] International Towing Tank Conference, 2021. Recommended Procedures and Guidelines 7.5-02-07-02.1, Seakeeping Experiments.
- [34] Sanada, Y., Simonsen, C., Otzen, J., Sadat-Hosseini, H., Toda, Y., Stern, F., 2021. Experimental Data for KCS Added Resistance and ONRT Free Running Course Keeping/Speed Loss in Head and Oblique Waves. *Numerical Ship Hydrodynamic: An Assessment of the Tokyo 2015 Workshop*. 61-137. https://doi.org/10.1007/978-3-030-47572-7_4
- [35] Halder, P., Liu, S., 2024. A comprehensive unsteady RANS numerical investigation to unveil the influence of wave steepness on the motion dynamics and added resistance of a ship in waves. *Ocean Engineering*. 310, 118762. <https://doi.org/10.1016/j.oceaneng.2024.118762>
- [36] International Towing Tank Conference, 2014. Recommended Procedures and Guidelines 7.5-03-02-03, Practical Guidelines for Ship CFD Applications.
- [37] FINE™/Marine 11.2. Theory Guide. www.cadence.com
- [38] Kim, Y., Kim, J. H., 2016. Benchmark study on motions and loads of a 6750-TEU containership. *Ocean Engineering*, 119, 262-273. <https://doi.org/10.1016/j.oceaneng.2016.04.015>
- [39] International Towing Tank Conference, 2008. Recommended Procedures and Guidelines 7.5-02-07-02.1, Testing and Extrapolation Methods Loads and Responses, Seakeeping Experiments.
- [40] International Organization for Standardization, 2024. ISO15016. Ships and marine technology-Specifications for the assessment of speed and power performance by analysis of speed trial data.
- [41] Liu S., Low, M.C., Low, W.C., Chen, H.L., Shang, B.G., Papanikolaou, A., 2020. Rational processing of monitored ship voyage data for improved operation. *Applied Ocean Research*, 104, 102363. <https://doi.org/10.1016/j.apor.2020.102363>
- [42] Vinayak, P. P., Prabu, C. S. K., Vishwanath, N., Prakash, S. O., 2021. Numerical simulation of ship navigation in rough seas based on ECMWF data. *Brodogradnja*, 72(1), 19-58.

APPENDIX

FFT Analysis of Additional Cases

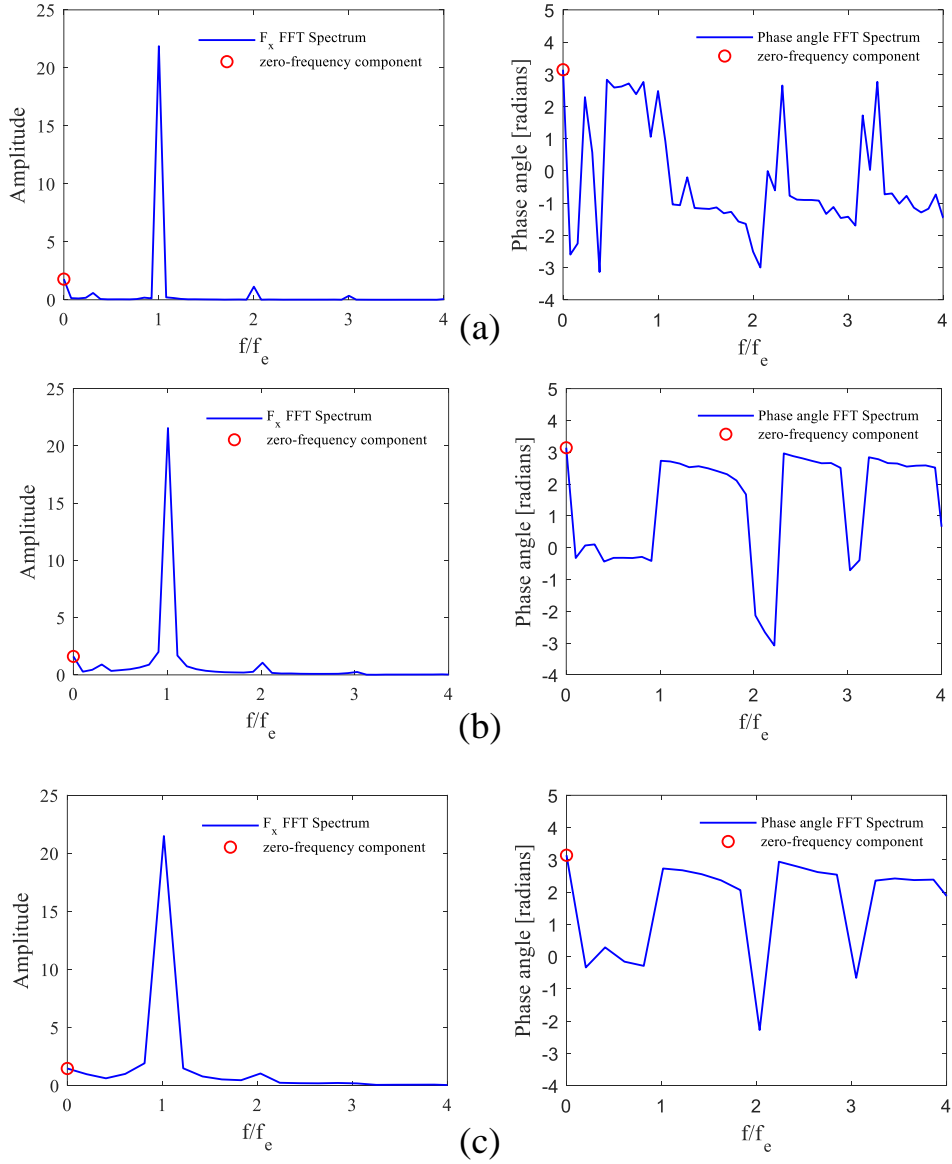


Fig. A1 FFT analysis results using the data of (a) 13, (b) 10 and (c) encounter periods, respectively. $\lambda/L_{PP}=0.50$, and $Fn=0.15$

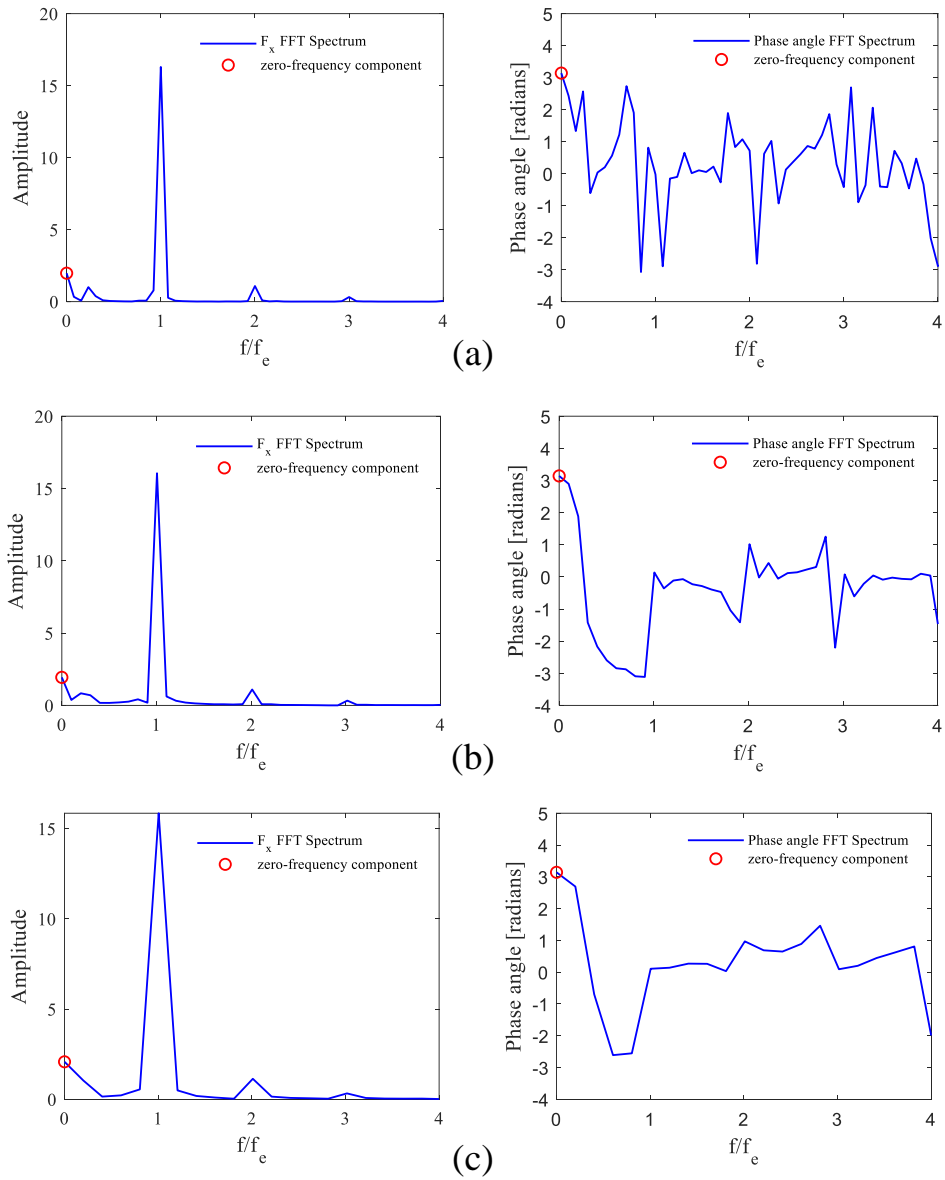


Fig. A2 FFT analysis results using the data of (a) 13, (b) 10 and (c) 5 encounter periods, respectively. $\lambda/L_{PP}=0.40$, and $Fn=0.15$

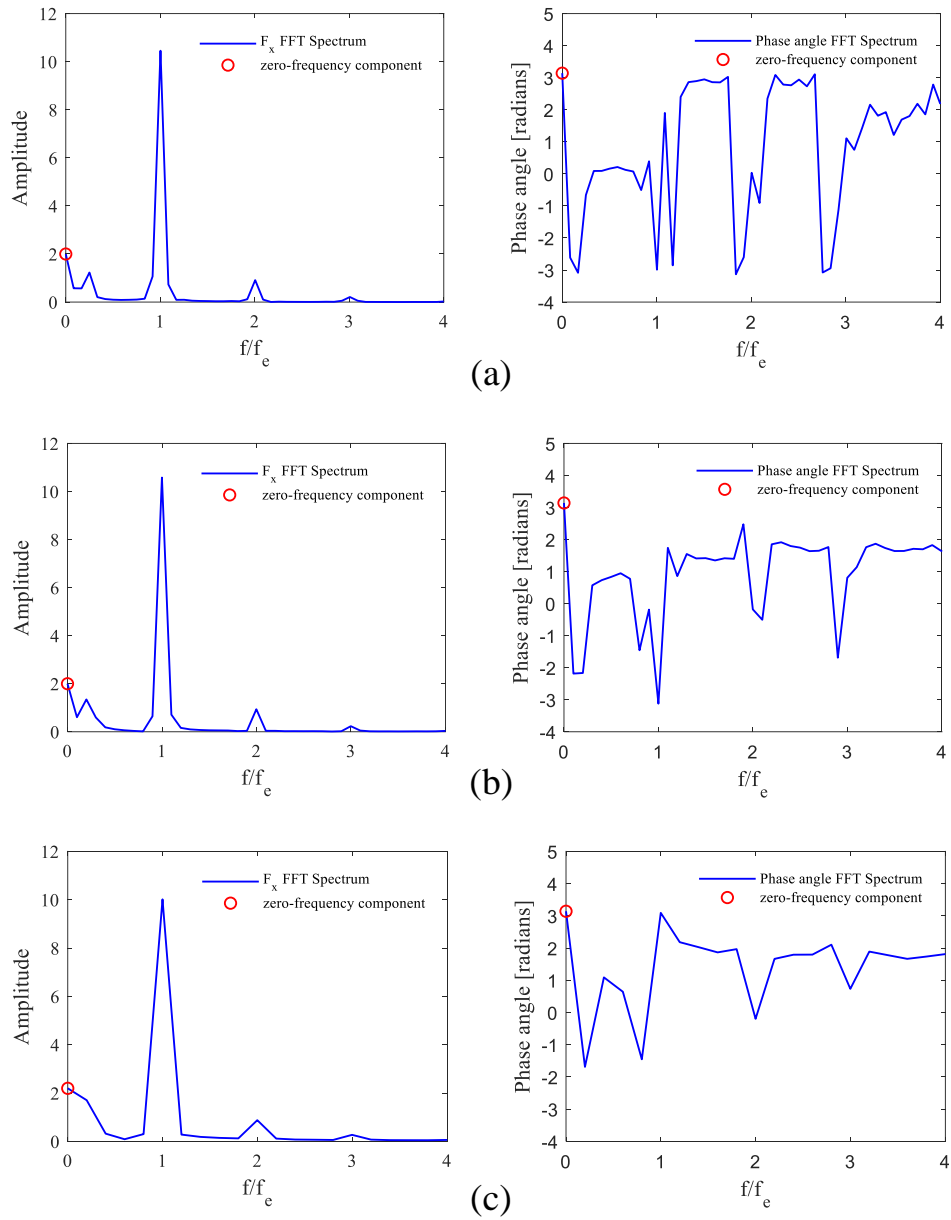


Fig. A3 FFT analysis results using the data of (a) 12, (b) 10 and (c) 5 encounter periods, respectively. $\lambda/L_{PP}=0.33$, and $Fn=0.15$

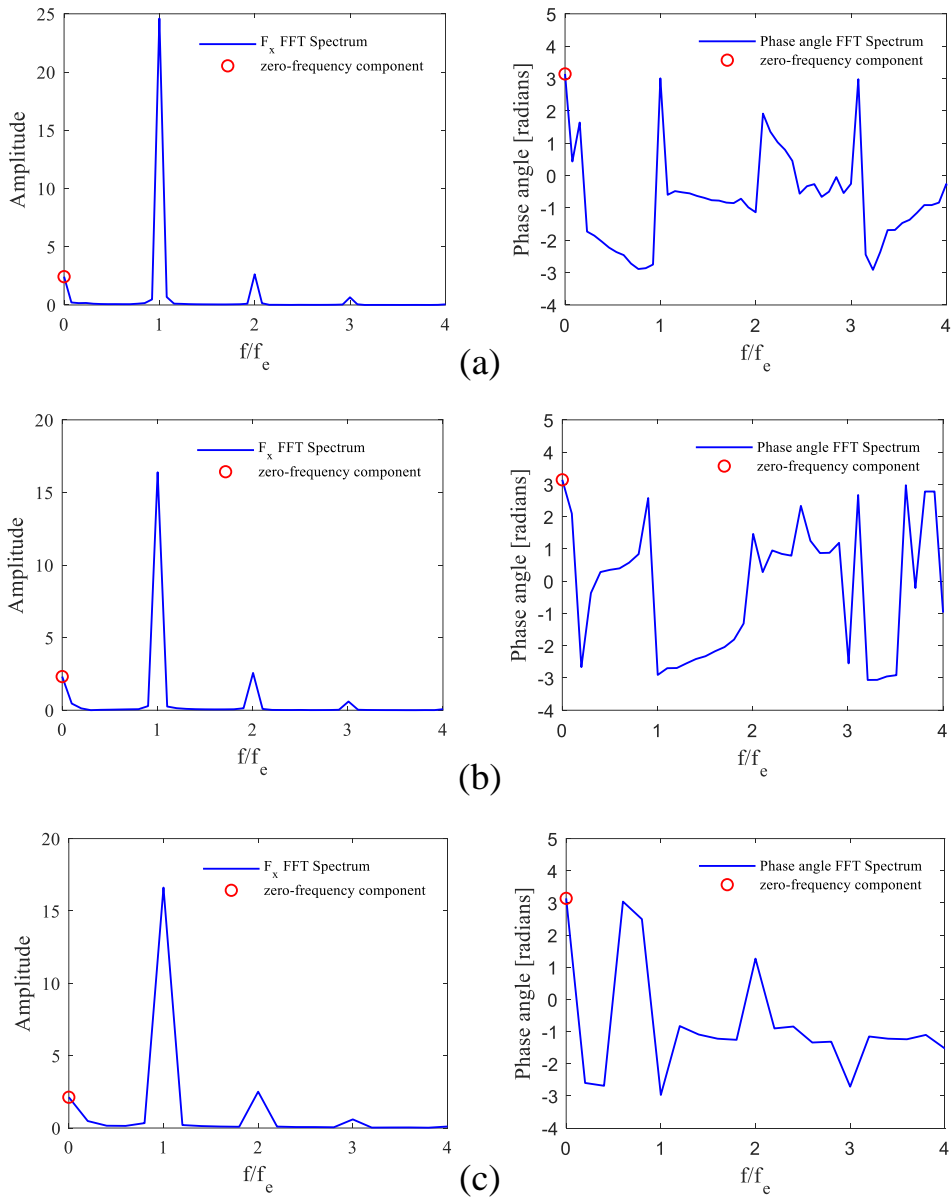


Fig. A4 FFT analysis results using the data of (a) 13, (b) 10 and (c) 5 encounter periods, respectively. $\lambda/L_{pp}=0.50$, and $Fn=0.26$

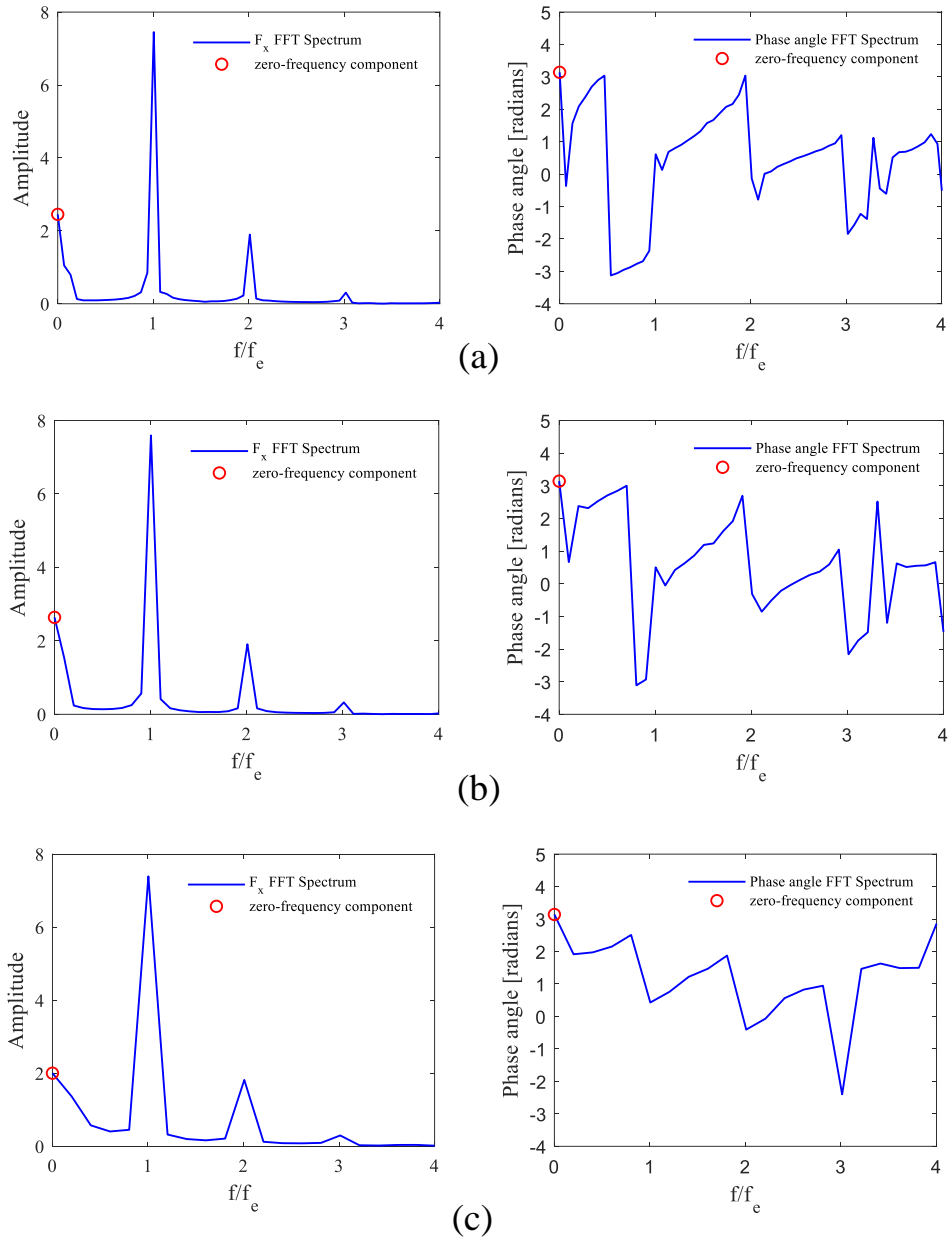


Fig. A5 FFT analysis results using the data of (a) 15, (b) 10 and (c) 5 encounter periods, respectively. $\lambda/L_{pp}=0.33$, and $Fn=0.26$